SANDIA REPORT

SAND83—1788 • UC—45
Unlimited Release
Printed January 1988

Transient Compressible Flow in Porous Materials

J. E. Shepherd, D. R. Begeal

Prepared by
Sandia National Laboratories
Albuquerque, New Mexico 87185 and Livermore, California 94550
for the United States Department of Energy
under Contract DE-AC04-76DP00789

SF2900Q(8-81)

Issued by Sandia National Laboratories, operated for the United States Department of Energy by Sandia Corporation.

Printed in the United States of America
Available from
National Technical Information Service
U.S. Department of Commerce
5285 Port Royal Road
Springfield, VA 22161

NTIS price codes
Printed copy: A04
Microfiche copy: A01

Distribution
UC-45

SAND83-1788
Unlimited Release
Printed January 1988

Transient Compressible Flow

in

Porous Materials*

J. E. Shepherd
Fluid Mechanics and Heat Transfer Division
and
D. R. Begeal
Explosive Subsystems Division

Sandia National Laboratories
Albuquerque, NM 87185
Operated by
Sandia Corporation
for the
U. S. Department of Energy

Abstract

An experimental investigation of transient compressible flow in porous materials is reported. Two types of experiments have been carried out to verify the simplified models of compressible flow that have been developed by other investigators over the last decade and to extend the drag coefficient measurements to high Reynolds numbers. Results are reported for packed beds contructed from glass beads and three types of granular explosives: CP, HMX, and HNS.

---

*This work performed at Sandia National Laboratories supported by the U. S. Dept. of Energy under contract number DE-AC04-76DP00789.

Contents

List of Figures

List of Tables

Executive Summary

An experimental investigation of transient compressible flow in porous materials is reported. Two types of experiments have been carried out to verify the simplified models of compressible flow that have been developed by other investigators over the last decade and to extend the drag coefficient measurements to high Reynolds numbers. Results are reported for packed beds constructed from glass beads and three types of granular explosives: CP, HMX, and HNS.

In the first type of experiment, a reservoir of high-pressure nitrogen gas is blown down through packed beds of both inert and explosive materials. We show that after an initial transient, the gas flow becomes quasi-steady and the drag coefficient can be deduced from the pressure-time history of the reservoir gas. Using this technique, the drag coefficient can be determined over a large range of Reynolds numbers in a single test. Results are reported for Reynolds numbers from 10^{-4} to 10^{5} and compared with the conventional drag coefficients reported by previous investigators.

In the second type of experiment, a miniature shock tube has been used to impulsively apply nitrogen gas at pressures from 100 to 20,000 psia to a bed of packed glass beads instrumented with pressure transducers. Glass beads with mean diameters ranging from 5 to 300 μm were used. The results of these experiments are compared to numerical solutions of the proposed model equations and simple analytic models that result at large and small Reynolds numbers.

1 Introduction

1.1 Motivation

The flow of a fluid through a porous medium is an important physical process. Considerable work has been done in the fields of hydrology, petroleum engineering, and filtration, where the fluids are liquid. Drying operations and the burning of propellants are two examples where the fluid is a gas. Our particular interest is application to the burning of pyrotechnics and the transition from deflagration to detonation in porous (granular) explosives. These materials have very small particle sizes, and extremely high gas pressures and velocities can be generated during combustion. For these reasons, the characteristic Reynold's number for the gas flow can be several orders of magnitude larger than any achieved in previous experiments.

In order to extend the existing experimental data base to a higher Reynold's number range, we have developed two new techniques for measuring gas permeability in porous columns. Experiments were performed on idealized particulate beds (glass spheres) to establish the methods and to verify existing correlations. More complex materials were used to assess the usefulness of these correlations on nonideal, granular materials. These materials were the granular explosives CP, HMX, and HNS.

The organization of the report is as follows. First, we briefly review the theoretical basis of gas flow in rigid porous materials. Second, the materials used in this study are described. Third, the quasi-steady technique for measuring permeability is presented; results for glass beads and explosives are given. Fourth, the pulse method for determining permeability is presented and results for glass beads discussed. Finally, the results of both quasi-steady and pulse measurements are compared.

1.2 Review

The theoretical basis of porous fluid flow is described in detail by Dullien.[1] An excellent review of existing experimental work on permeability measurement is given by McDonald *et al.*[2] The basis of almost all theoretical treatments of gas flow in a rigid porous bed is the continuity equation

$$\epsilon \frac{\partial \rho}{\partial t} + \frac{\partial \rho u}{\partial x} = 0 \tag{1}$$

and some approximate model of the momentum equation, e.g., the Forchheimer equation

$$-\frac{\partial p}{\partial x} = \alpha \mu u + \beta \rho u^2 \tag{2}$$

where p is the gas pressure, ρ the gas density, u the "filtration" velocity of the gas (volume flow rate divided by bed cross-sectional area), ϵ the bed porosity, and μ the fluid viscosity. If there are large temperature differences between the fluid and the solid

phases, then the coupled energy equations for both phases must be considered. For the flows we will consider, the fluid–solid temperature differences can be shown to be small and the gas flow can be considered isothermal. The constants α and β are functions of the properties of the porous material and have to be experimentally determined in order to complete this model. The usual procedure is to define two other constants, the permeability κ and the Forchheimer constant λ, which are defined as

$$\kappa = \frac{1}{\alpha}, \tag{3}$$

$$\lambda = \kappa\beta. \tag{4}$$

The Forchheimer model for the momentum equation is a very simple description of the force balance in the flow. The inertial terms are neglected in the gas momentum equation and pressure drop is balanced against a drag force composed of a viscous and an inertial term. Neglecting the flow inertia implies that shock waves and other nonlinear gasdynamic phenomena such as choking are neglected. These omitted terms can be shown to be unimportant in the experiments we describe. A particular form of the drag law is also used in Eq. 2; many variations on this form have been employed by different researchers.

A generalized form of Eq. 2 can be written in terms of a drag law by defining a drag coefficient C_D and a Reynolds number Re based on the characteristic particle size d of the porous material,

$$C_D = \frac{-\partial p/\partial x}{\rho u^2/d} \tag{5}$$

and

$$Re = \frac{\rho u d}{\mu} \tag{6}$$

The general form of the drag law is some functional dependence of the drag coefficient on the Reynolds number and the parameters describing the porous material.

$$C_D = C_D\left(Re, \epsilon, d, \ldots\right) \tag{7}$$

This result follows from dimensional analysis for subsonic continuum flows since Re and C_D are the only important nondimensional parameters under these circumstances. The Forchheimer form of the drag law can be rearranged to yield a drag coefficient of the general form,

$$C_D = \frac{d^2}{\kappa}\left(\frac{1}{Re} + \frac{\lambda}{d}\right). \tag{8}$$

Representing the drag law in this form clearly shows the dependence on Reynolds number. At low Reynolds numbers, the drag coefficient has the Re^{-1} dependence characteristic of any highly viscous fluid flow. At high Reynolds numbers, the drag coefficient is independent of Reynolds number as also found in conventional high–speed fluid flow. While this postulated Reynolds number dependence has the correct qualitative behavior at the extremes of the flow regimes, the exact form of the dependence for particular porous materials may vary. In particular, the behavior at very high Reynolds numbers has been little explored and the approach to infinite Reynolds number is poorly understood.

Examples of typical data reduction techniques and expressions for κ and κ/λ are given in MacDonald *et al.*[2] For porous materials composed of packed spherical particles, they show that all data can be adequately correlated by the Carman–Kozeny expression for the permeability

$$\kappa_m = \frac{\bar{d}^2\epsilon^3}{180(1-\epsilon)^2} \tag{9}$$

and the Ergun relation for the Forchheimer constant

$$\frac{\kappa_m}{\lambda_m} = \frac{\bar{d}\epsilon^3}{1.8(1-\epsilon)} \tag{10}$$

where ϵ is the porosity (volume fraction of pore space) of the bed and $\bar{d}$ is the surface–averaged particle diameter computed from the distribution $n(d)$ of particle sizes:

$$\bar{d} = \frac{\int_0^\infty \phi^3 n(\phi)d\phi}{\int_0^\infty \phi^2 n(\phi)d\phi}. \tag{11}$$

Rumpf and Gupte[3] were able to fit their data better using only the viscous portion of Eq. 7 with a correlation of

$$\kappa_{rg} = \frac{\bar{d}^2\epsilon^{5.5}}{5.6K}. \tag{12}$$

The constant K depends on the particle morphology; Rumpf and Gupte found that $K = 1$ for spherical particles. This was true for beds containing spheres with a wide distribution of sizes with a porosity range $0.35 \leq \epsilon \leq 0.7$. As many researchers have pointed out, the porosity functions will depend not only on the particle size distribution, but also on the particle shape and resulting packing structure. For any particular material, the problem is to experimentally obtain enough data to determine $C_D(Re)$ over the range in Reynolds numbers of interest in the particular application. For certain types of materials it is then possible to represent the drag law with an existing correlation such as Eq. 7 and extract the parameters used in the correlation. This is the approach used in the present work.

2 Materials

Experiments were conducted on two types of porous materials, inert and explosive. Both materials were formed into packed beds from the original loose powder or granular state. The inert material used was spherical glass beads, referred to as GB throughout this report. The explosive materials were CP, HMX, and HNS. CP is a relatively new explosive[4] in which a combustion wave can easily transition from a deflagration to a detonation, referred to as DDT (deflagration–to–detonation transition). The behavior of DDT in CP has been investigated both experimentally and theoretically and the results are given in Ref. 5. HMX is a commonly used research explosive that also exhibits DDT behavior. A classic study on DDT in HMX as a function of permeability and particle size was performed by Groocock and Griffiths.[6] HNS is a relatively insensitive explosive in which the permeability is thought to play a minor role.

2.1 Glass Bead Beds

Five lots of commercially available spherical glass beads were used. Each lot had a different mean size and distribution; mean diameters of 284, 167, 111, 14, and 3 μm were used. The glass density of each lot was determined by air picnometry, and the surface–averaged particle diameter $\bar{d}$ was determined by Quantimet[7] analysis of SEM photographs of the beads. The actual distributions obtained for each lot are shown in Figs. 1-3. The bimodal distribution found with the 111 μm lot was clearly due to a mixture of distinctly different size beads.

Packed beds were prepared in 4.76 mm diameter tubes that were closed at the bottom by either a pressure transducer for shock–tube experiments or porous metal frits for quasi-steady–state experiments. A weighed quantity of spheres was poured into the tube while holding a vibrator against the side of the tube to aid in compaction and settling of the spheres. In the terminology quoted by Dullien[1], this results in a "close random packing" structure of the bed. Porosities of these beds were almost all between 0.3 and 0.4.

Usually, the spheres in the packed configuration were free–flowing and the bed was handled carefully and always kept vertical to avoid disturbing the original packing. The final bed length in the tube was measured and used to compute the bed porosity. Note that for some beds there was additional settling during experimentation; this was accounted for in reducing the data. Information regarding the beds (density, porosity, and length) is given in Table 1. The results of the experiments are given for later reference.

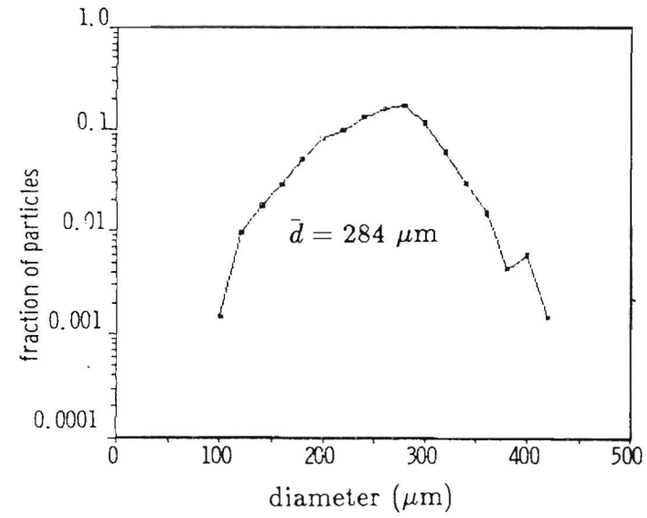

(a)

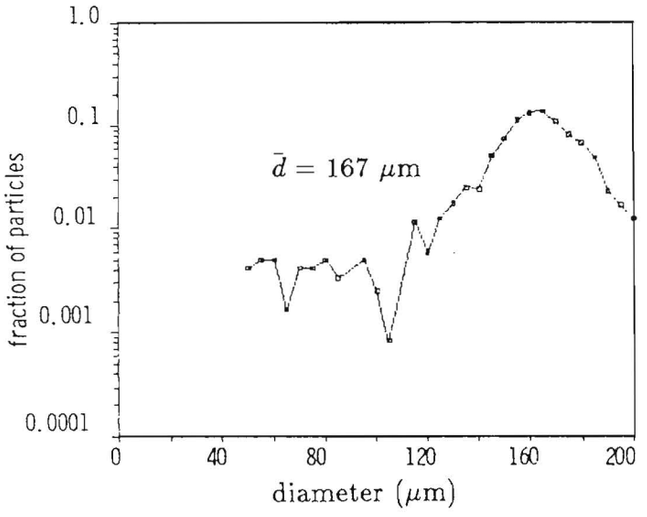

(b)

Figure 1: Particle size distributions for glass beads. (a) 287 μm diameter lot. (b) 167 μm diameter lot.

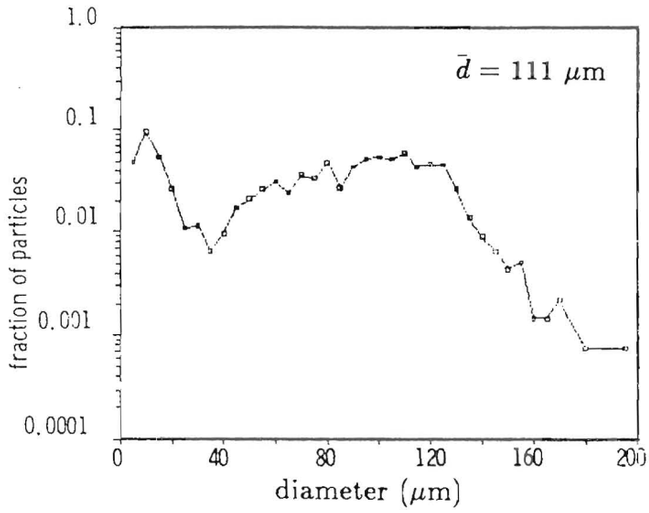

(a)

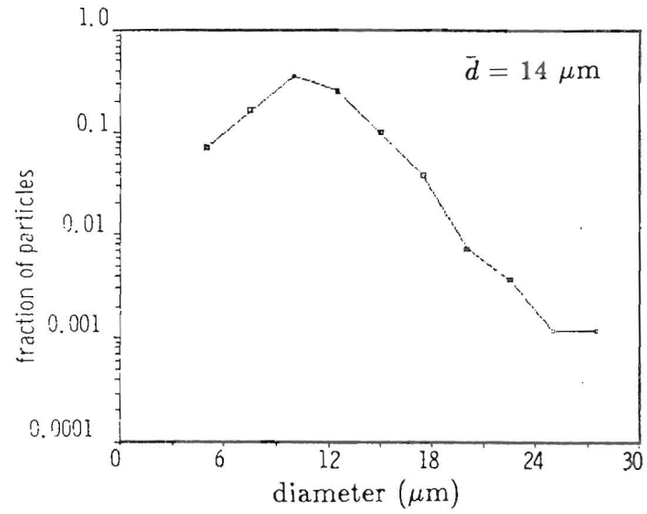

(b)

Figure 2: Particle size distributions for glass beads. (a) 111 μm diameter lot. (b) 14 μm diameter lot.

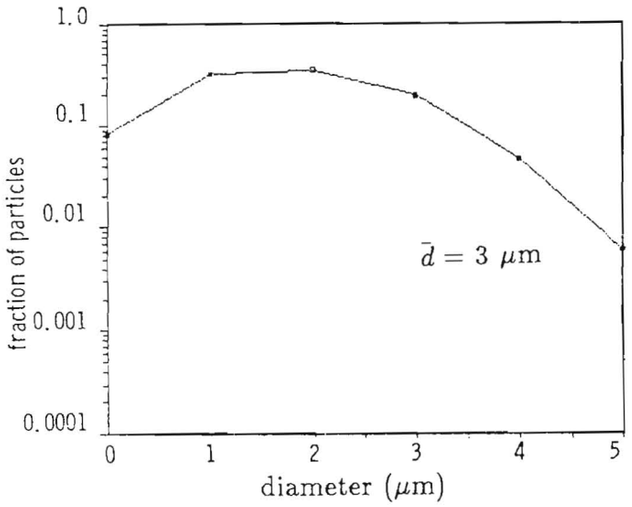

Figure 3: Particle size distributions for glass beads. 3 μm diameter lot.

Table 1: Glass Bead Packed Bed Parameters

$\bar{d}$ (μm)	TMD* (g/cm^3)	ϵ	L (cm)	κ (cm^2)	κ_m (cm^2)	κ_{rg} (cm^2)	κ/λ (cm)	κ_m/λ_m (cm)
284	2.74	0.350	12.6	7.2×10^{-7}	4.6×10^{-7}	4.4×10^{-7}	5.4×10^{-3}	3.0×10^{-3}
		0.348	25.2	6.8×10^{-7}	4.4×10^{-7}	4.3×10^{-7}	4.1×10^{-3}	2.9×10^{-3}
		0.336	40.1	7.2×10^{-7}	3.9×10^{-7}	3.6×10^{-7}	4.4×10^{-3}	2.7×10^{-3}
		0.332	55.3	7.6×10^{-7}	3.7×10^{-7}	3.3×10^{-7}	4.1×10^{-3}	2.6×10^{-3}
167	2.39	0.354	18.2	3.6×10^{-7}	1.6×10^{-7}	1.6×10^{-7}	2.5×10^{-3}	1.8×10^{-3}
		0.358	33.0	4.1×10^{-7}	1.7×10^{-7}	1.7×10^{-7}	2.4×10^{-3}	1.9×10^{-3}
111	2.74	0.290	31.1	1.4×10^{-7}	3.3×10^{-8}	2.4×10^{-8}	1.7×10^{-3}	7.3×10^{-4}
14	2.35	0.400^{BP}	19.8	6.9×10^{-9}	1.9×10^{-9}	2.3×10^{-9}	2.6×10^{-4}	2.1×10^{-4}
		0.294^{AP}	19.9	4.9×10^{-9}	5.6×10^{-10}	4.2×10^{-10}	1.2×10^{-4}	9.5×10^{-5}
		0.288^{AP}	30.2	3.9×10^{-9}	5.1×10^{-10}	3.7×10^{-10}	7.4×10^{-5}	9.1×10^{-5}
3	2.48	0.311^{AP}	5.0	1.6×10^{-10}	3.2×10^{-11}	2.6×10^{-11}	1.7×10^{-7}	2.3×10^{-5}
		0.325^{AP}	8.4	1.8×10^{-10}	3.8×10^{-11}	3.3×10^{-11}	3.4×10^{-7}	2.6×10^{-5}

*Theoretical Maximum Density
BP – before pulse conditioning
AP – after pulse conditioning

2.2 Granular Explosives

Packed beds of explosive materials were prepared by pressing increments of powder into a plugged, precision–bore, steel tube. The pressing was performed with a precision–machined ram that was forced into the tube, on top of loose powder, with hydraulic pressure. With this procedure, columns of explosive could be pressed in place or a free standing pellet could be formed by removing the plug and forcing the compressed material out of the tube. The powder compaction was controlled by pressing to a fixed height or by using a constant ram pressure. We used the later approach in this work. The powder weight for the increments were kept nearly the same, and were such that when the desired ram pressure was applied, the resulting increment had a length to diameter ratio of 0.5 or less. Careful records of sample weight and increment heights were maintained for eventual porosity determinations.

2.2.1 CP

CP, unlike most explosives, is inorganic in nature. That is, CP crystals are hard and tend to fracture under stress, whereas HMX tends to be mushy and will smear or deform prior to fracturing. CP powder is prepared by crash precipitating an aqueous solution into cold isopropyl alcohol. The degree of crashing has an effect on the precipitated crystal size. We used four different materials, three of typical production particle size and one with abnormally large crystals. All materials were in the form of agglomerated crystals; however, upon mild pressing, the agglomerates were broken up. Under severe pressing, even the crystals are fractured, therefore the size and packing structure of the individual particles in the pressed state can be very different than in the virgin state.

A typical packed bed of CP was 2 mm in diameter and 20 mm long. This required 20 pressing steps in 1 mm increments. We used packed beds of densities ranging from 1.4 to 1.9 g/cm^3 with each lot of material. Since CP has a theoretical maximum density (TMD) of 2.0 g/cm^3, this is equivalent to porosities of 0.3 to 0.05. This yields a slight overlap with the range of porosity obtained with the GB beds. Unlike the GB beds, CP beds were self–supporting and no metal frit was needed in the beds used for quasi–steady–state measurements.

Along with the beds, companion free–standing pellets were pressed. These pellets were dispersed in isopropyl alcohol and then analyzed with the Quantimet for particle size distributions of the material in the pressed state. Figures 4-7 show the SEM photographs and distributions for two lots. Lot EL41088 consisted of abnormally large crystals, 29 μm $\leq \bar{d} \leq$ 155 μm. Lot EL47344 consisted of more normal size crystals, $\bar{d} \simeq$ 10 μm. This lot was more typical of the production material and the other two lots used in this study.

SEM photographs of the virgin (unpressed) material are also shown. Note the rounding effect of the ultrasonic dispersion process and the large number of small particles produced by the pressing process. Clearly, pressing dramatically alters the original shapes and sizes. The higher the ram pressure, the higher the final density,

the lower the porosity and the greater the alteration of the particle shapes and sizes. CP packed–bed parameters are given in Table 2.

The individual CP particles are very irregular in shape and will therefore have a very different packing structure than the spherical GB. For this reason, the mean diameter is not as significant a descriptor of the pore structure and we expect that a different correlation of permeability will be obtained for CP than for GB. One of the primary purposes of the present investigation was to determine these differences between the classical correlations for spherical particles and the experimental correlations for granular explosives.

Table 2: CP Packed–Bed Parameters

$\bar{d}$ (μm)	ϵ	L (cm)	κ (cm^2)
		Lot EL41088	
-	0.275	2.5	7.1×10^{-10}
-	0.125	2.5	8.0×10^{-13}
149	0.260	2.0	7.0×10^{-10}
63	0.150	2.0	6.8×10^{-12}
29	0.090	2.0	1.1×10^{-13}
79	0.030	2.0	2.6×10^{-15}
		Lot EL47344	
-	0.275	2.5	2.4×10^{-11}
-	0.200	2.5	2.4×10^{-12}
-	0.125	2.5	2.2×10^{-13}
10.4	0.300	2.0	3.7×10^{-11}
7.7	0.190	2.0	4.1×10^{-12}
8.3	0.160	2.0	8.2×10^{-13}
9.6	0.110	2.0	1.0×10^{-13}

$L = 2.5$ cm beds had an area of
$A = 0.094$ cm^2
$L = 2.0$ cm beds had an area of
$A = 0.080$ cm^2

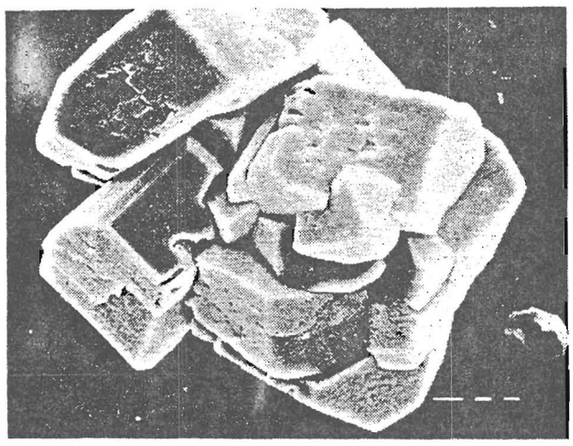

— 10 microns

(a)

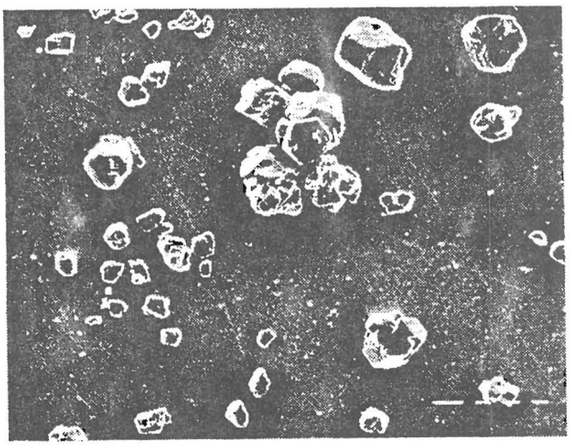

— 100 microns

(c)

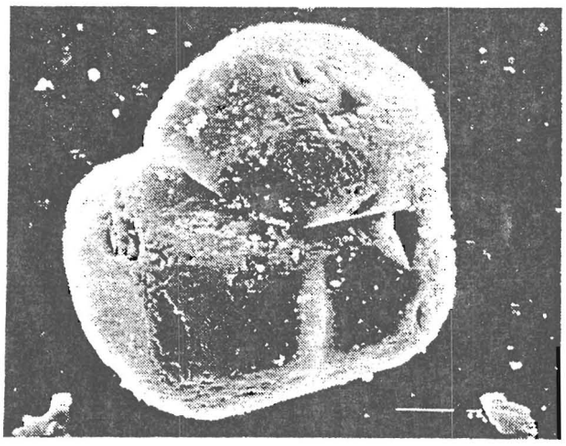

—— 10 microns

(b)

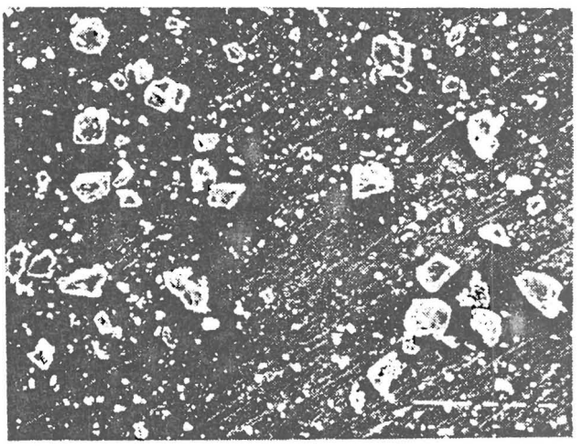

—— 100 microns

(d)

Figure 4: SEM Photographs of CP lot EL-41088 (abnormally large crystals). (a) Virgin. (b) Virgin, after ultrasonic dispersion. (c) Pressed, $\rho = 1.44$ g/cm^3, ultrasonically dispersed. (d) Pressed, $\rho = 1.82$ g/cm^3, ultrasonically dispersed.

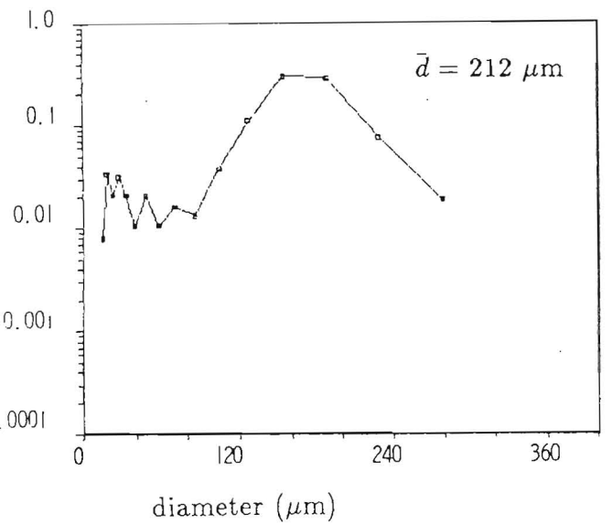

(a)

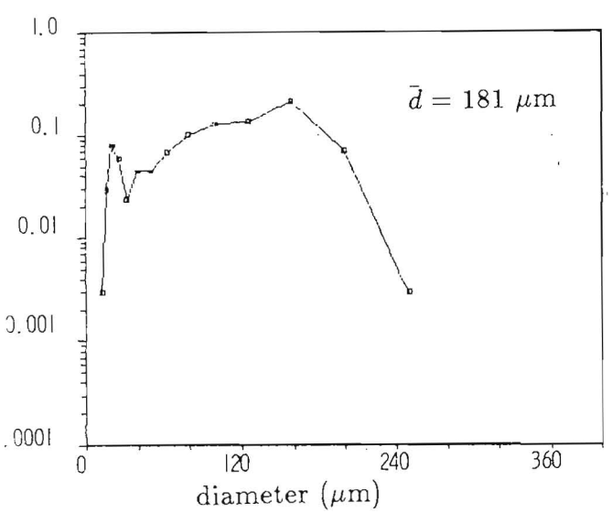

(b)

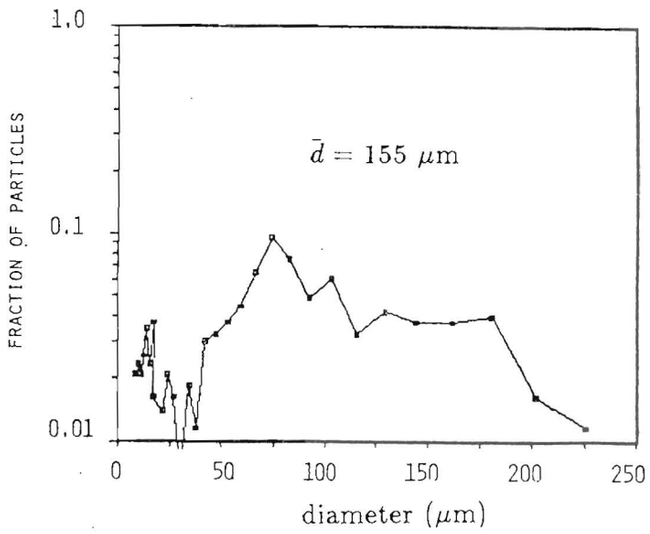

(c)

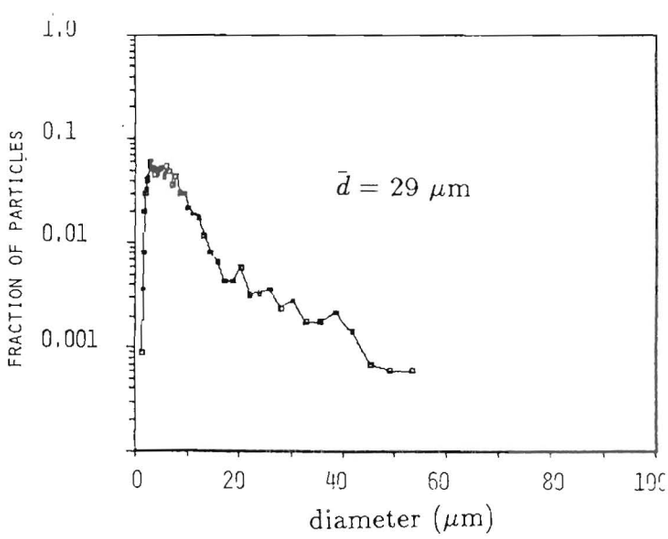

(d)

Figure 5: Size distributions of CP lot EL-41088 (abnormally large crystals). (a) Virgin. (b) Virgin, after ultrasonic dispersion. (c) Pressed, ρ = 1.44 g/cm^3, ultrasonically dispersed. (d) Pressed, ρ = 1.82 g/cm^3, ultrasonically dispersed.

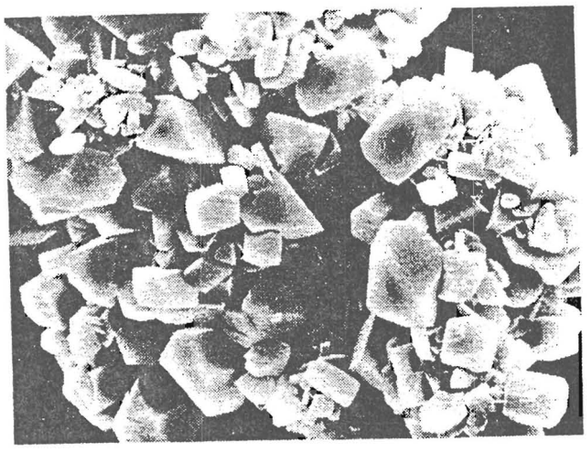

—— 10 microns

(a)

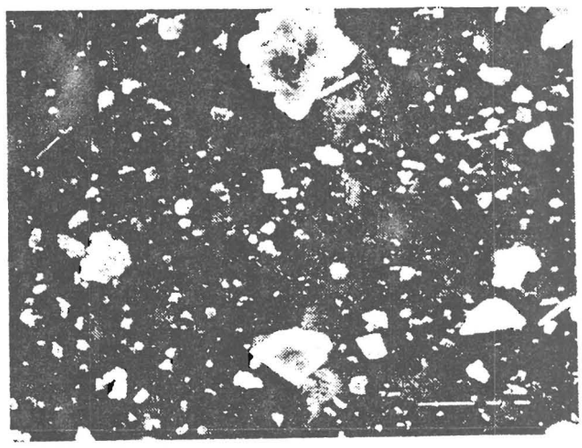

—— 10 microns

(c)

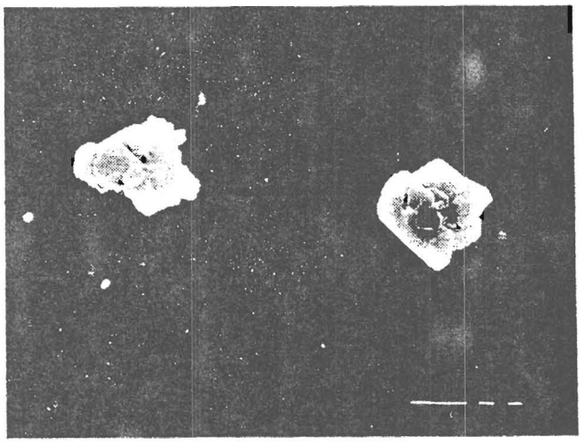

—— 10 microns

(b)

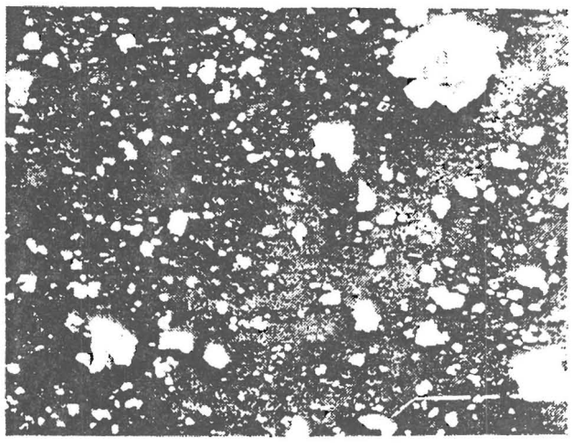

—— 10 microns

(d)

Figure 6: SEM photographs of CP lot EL-47344 (normal crystal size). (a) Virgin. (b) Virgin, after ultrasonic dispersion. (c) Pressed, $\rho = 1.41$ g/cm^3, ultrasonically dispersed. (d) Pressed, $\rho = 1.78$ g/cm^3, ultrasonically dispersed.

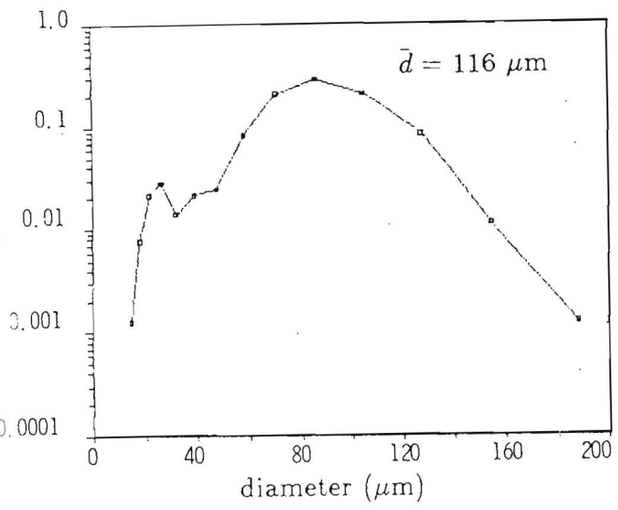

(a)

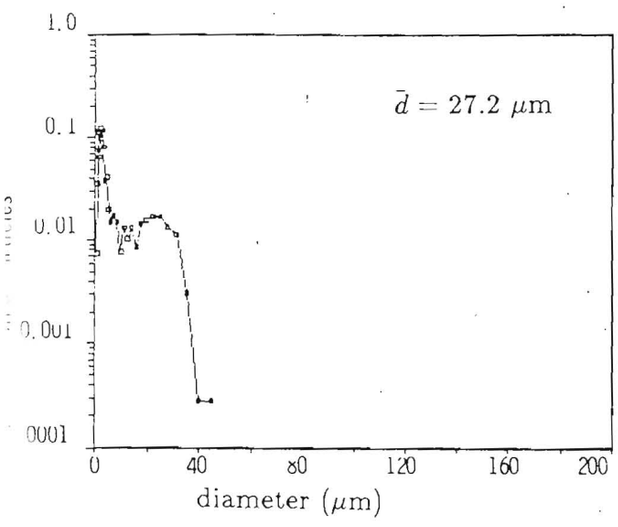

(b)

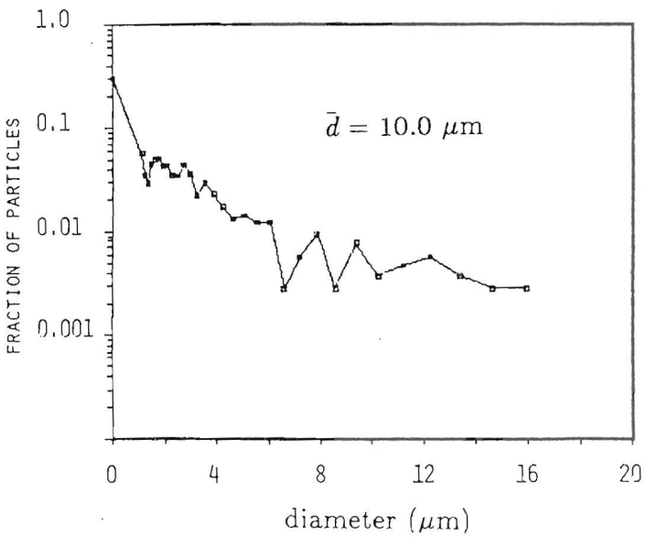

(c)

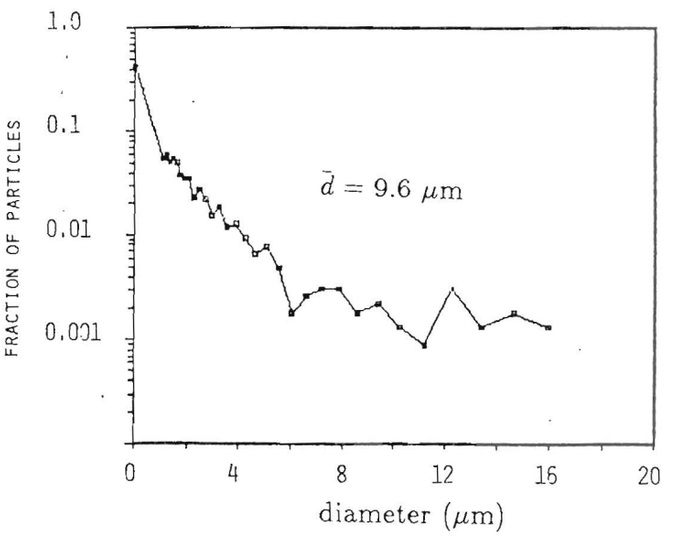

(d)

Figure 7: Size distributions of CP lot EL-47344 (normal crystal size). (a) Virgin. (b) Virgin, after ultrasonic dispersion. (c) Pressed, ρ = 1.41 g/cm^3, ultrasonically dispersed. (d) Pressed, ρ = 1.78 g/cm^3, ultrasonically dispersed.

2.2.2 HMX

A limited number of experiments on HMX were performed. The material used was of unknown purity and manufacture. Permeability measurements were made on 10 samples pressed to porosities ranging from 0.05 to 0.21. This corresponds to densities ranging from 1.8 to 1.5 g/cm^3; TMD is 1.905 g/cm^3. Two diameter fixtures were used: one 0.254 cm in diameter, the other 0.32 cm in diameter. Particle size distributions were not determined for this material. Bed parameters and experimental results are tabulated in Table 3.

Table 3: HMX Packed–Bed Parameters

ϵ	ρ (g/cm^3)	κ (cm^2)
	0.32 cm in diameter	
0.213	1.502	3.4×10^{-10}
0.186	1.560	6.0×10^{-11}
0.160	1.607	5.3×10^{-11}
0.160	1.598	5.8×10^{-11}
0.118	1.679	2.0×10^{-12}
0.110	1.695	3.3×10^{-12}
	0.254 cm in diameter	
0.200	1.524	5.0×10^{-10}
0.162	1.597	1.1×10^{-10}
0.094	1.725	5.5×10^{-13}
0.046	1.817	2.3×10^{-13}

0.32 cm diameter beds had an average length of 2.0 cm
0.254 cm diameter beds had an average length of 1.8 cm

2.2.3 HNS

A limited number of experiments were also carried out with HNS. The materials used included Type I, Type IIa, and HF (Hyper–Fine). Only the permeability results are available. Data were obtained for densities from 1.36 to 1.76 g/cm^3; TMD is 1.74 g/cm^3. This corresponds to a porosity range of 0.22 to 0.0. The bed parameters and experimental results are given in Table 4.

Table 4: HNS Packed–Bed Parameters

ϵ	ρ (g/cm^3)	κ (cm^2)
	Type I	
0.218	1.36	1.6×10^{-12}
0.140	1.50	2.7×10^{-13}
0.072	1.62	1.0×10^{-14}
0.063	1.64	1.4×10^{-14}
0.011	1.73	$< 10^{-15}$
	Type IIA	
0.193	1.40	2.5×10^{-11}
0.140	1.50	5.8×10^{-12}
0.098	1.57	1.8×10^{-12}
0.069	1.62	1.2×10^{-13}
0.0	1.76	$< 10^{-15}$
	Type HF	
0.195	1.40	8.7×10^{-14}
0.177	1.43	7.9×10^{-14}
0.126	1.52	3.0×10^{-14}
0.063	1.63	$< 10^{-15}$

3 Quasi–Steady–State (QSS) Experiments

3.1 Apparatus and Techniques

The overall layout of the experimental apparatus is shown in Fig. 8. The apparatus consisted of a gas supply system, a gas reservoir, rupture disk, the packed bed fixture, pressure transducers and recording equipment. Essentially the same equipment was used for both the pressure–pulse and QSS experiments. The common feature of the apparatus for both types of experiments was the gas supply system. Gas plumbing was constructed entirely of stainless steel high–pressure hardware that was commercially available. Because explosives were used, the high–pressure and packed–bed sections of the apparatus were controlled remotely and contained in a test room approved for explosive operations. The valves were of the remotely operated, pneumatic type and were interlocked with a shield around the apparatus and the door to the testing room.

Bottled dry nitrogen was fed to the apparatus from outside the room with a manual valve, and the apparatus could also be vented to the atmosphere manually. The gas booster shown in Fig. 8 was used primarily in the pulse experiments. The apparatus was equipped with a safety rupture disc and an orifice for automatic venting. The attachment of the bed to the apparatus was at a common point for either type of experiment. Control lines and signal lines from the pressure transducers were fed outside the room to the remote control panel and the recording equipment.

The QSS experiment is essentially a constant–volume, blowdown technique. This means that a constant–volume reservoir of initially high–pressure gas was discharged through the length of the bed to atmospheric pressure. As described in more detail below, by measuring the pressure in the reservoir as a function of time, the drag coefficient for the packed bed can be determined over a range of Reynolds numbers defined by the total pressure drop. The technique is referred to as "quasi–steady" because the discharge rate is made slow enough that the flow through the bed is governed by the steady flow equations even though the reservoir pressure varies with time.

The effective reservoir volume is defined by the plumbing of the apparatus, the size of reservoir used, and the bed fixture. Volume was determined by $p - V$ comparisons against a calibrated volume that is part of the apparatus. The plumbing arrangement could easily be modified so that the total volume could be tailored to the particular bed. It is imperative that the flow of gas through the beds reach a quasi-steady-state in order for the data reduction to be valid. At the same time, we did not want prohibitively long blowdown times. At the two extremes, we used a volume of approximately 2 liters for the 284 μm GB beds, and a volume of a few milliliters for the most dense CP beds.

A schematic of the apparatus configuration for a QSS experiment is shown in Fig. 9a. Conceptually, the packed bed of porous material is attached at one end to the gas reservoir and open to the atmosphere at the other end. At the start of the experiment, the resevoir and bed were connected, resulting in gas flow between the high–pressure reservoir and the atmosphere. The pressure in the reservoir decreases continuously as

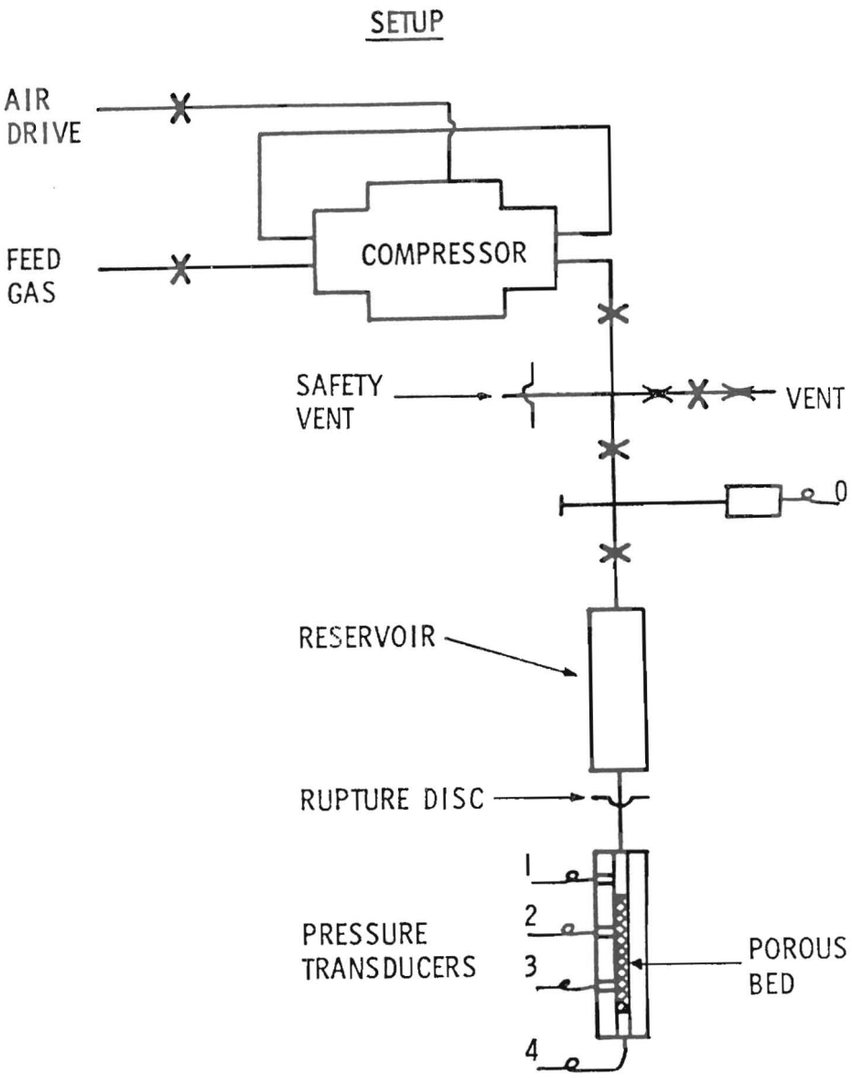

Figure 8: Overall layout of experimental apparatus for both QSS and pulse experiments

the gas flows through the packed bed towards the region of lower pressure. The experimental procedure was as follows. The effective reservoir volume of the apparatus upstream of the bed was determined and the packed bed was attached. The reservoir region was valved off from the bed and filled with dry nitrogen to the desired initial pressure. The ambient pressure was recorded and the valve between the reservoir and bed opened. Initially there was a surge of gas and a transient period as the gas flow through the bed approached quasi-steady-state. The experiment continued until the reservoir pressure approached the ambient pressure and gas flow ceased. The transient pressure in the known volume was measured by a commercial strain–gauge pressure transducer attached at a point between the valve and the bed. The pressure signal was recorded during the experiment with a digital oscilloscope. Typically, a total of 2048 data points were recorded for each run.

We found that it was necessary to condition the GB beds with a few high–pressure pulses prior to QSS experiments. These pulses would further compact the beds by a few percent with a corresponding reduction in permeability and porosity. Our usual procedure was to condition the bed, conduct the pulse experiments, convert the bed to the QSS configuration, conduct the QSS runs, and finally to conduct a few pulse runs after reconfiguration. To ease changing the bed from one configuration to another, the supporting pressure gauge and the frit were physically identical. We only needed to physically restrain the beads, invert the bed, and replace one support with the other. The last pulse runs were to insure that this manipulation did not disturb the bed. Several iterations of this procedure were used early in the investigations. We found that data on any single bed was reproduceable, regardless of sequence, after conditioning. We also were able to duplicate results on different beds that had been prepared in an identical fashion.

Our procedure with the explosive beds was different. Engaging or tightening threads in the presence of explosives is a hazardous procedure. The risk of igniting a loose particle that might be lodged between the threads is very real. For this reason, we decided to condition the explosive beds against the plug that was used during the pressing, and then to remove the plug for the QSS runs. The pulse runs were performed on a separate bed that was pressed against the pressure gauge. In this manner, we avoided threading into fixtures filled with explosives. As a safety precaution, the plug removal step was accomplished behind a blastshield, and other standard explosive safety practices such as grounding were observed. In all the experiments involving explosives, the sample size was kept to a minimum.

However, we found that during the initial conditioning, CP and HMX would ignite and undergo transition to detonation for pulses produced with reservoir pressures greater than 5000 psi. While this is a phenomenon that merits further investigation, we elected not to pursue it. The detonation products severely contaminated the apparatus and we were unable to collect any pulse data on the explosives that significantly extended the QSS results.

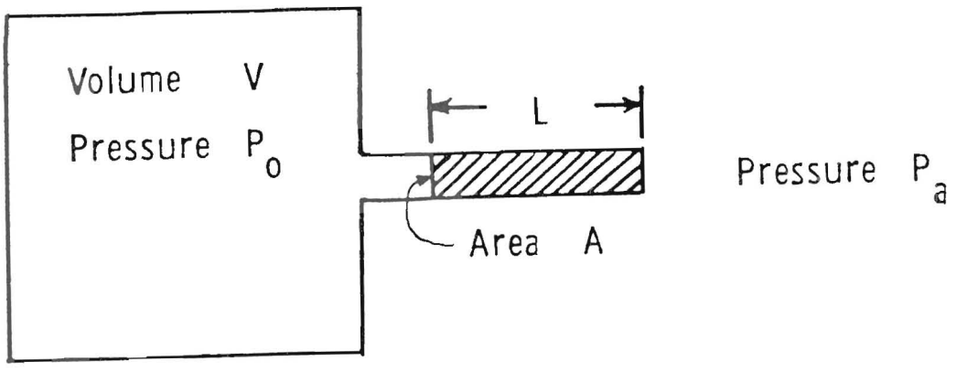

(a)

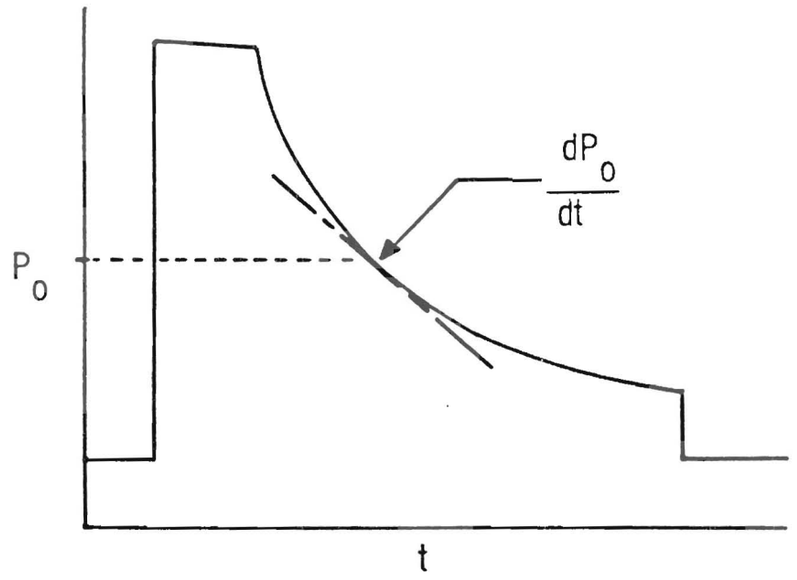

(b)

Figure 9: (a) Conceptual schematic of the apparatus arrangement for QSS experiments.
(b) Schematic of the pressure signal obtained in the QSS experiments.

4 QSS Theory and Data Reduction

In this section, we derive the expressions governing the quasi–steady flow of an ideal gas through a packed bed. The assumptions used in this derivation are that the gas obeys the ideal gas law, the absolute viscosity is independent of gas pressure, the gas flow is isothermal and governed by the continuum flow equations.

The first two assumptions depend strongly on the thermodynamic state of the gas, *i.e.*, the pressure and temperature. While nonideal effects are possible at the highest pressures (30,000 psi) used in these experiments, in practice these effects are assumed negligible. This is because the temperature (300 K) at which the experiments are carried out is 3 times the critical temperature of nitrogen (126 K). At 30,000 psi and 300 K, the compressiblity factor $Z = pV/RT$ differs from 1 by only 2.5%. The actual viscosity differs from the ideal gas value by a similar amount at these conditions.

The third assumption, isothermal flow, depends primarily on the rate of heat transfer between the gas and the packed bed. For the types of beds and gas flows considered in the present study, the heat transfer rates between the gas and bed are so high that the gas and bed are effectively in thermal equilibrium. Since the heat capacity of the bed is much higher than the total heat capacity of the gas that passed through during an experiment and the bed–gas temperature difference is small, thus the gas and bed remain at the initial bed temperature for the entire experiment.

The fourth assumption, continuum flow, depends on the Knudsen number Kn, defined as the ratio of the mean free path of the gas molecules to the characteristic flow dimension, *i.e.*, the mean pore size of the packed bed. In nitrogen, the mean free path at 300 K and 1 atm pressure is 0.25 μm. Since the pore sizes were not actually measured in the present study, we will assume that the characterisic pore size is similar to the mean particle size. The smallest sized particles used in the present study were of the order of 25 μm, implying a maximum value of $Kn = 0.01$. A typical criterion for continuum flow is that $Kn \leq 0.01$. Mean free path decreases with increasing pressure and therefore all experiments were performed in the continuum flow regime.

The continuum flow criterion is presented graphically in Fig. 10. This figure illustrates the relationship of the Knudsen number to the other important nondimensional parameters, the Reynolds number Re and the Mach number Ma. A generalized plot of this type is possible since for ideal gases the ratio of the Mach number to the Reynolds number is proportional to the Knudsen number. The range of the present experiments is given by the shaded region on the figure. Note that for all but the lowest Reynolds numbers, the flow is clearly in the continuum regime. Transition flows occur in explosives that have been pressed to very high density and have very small (2-5 μm) pore dimensions. Note that the flows are all very subsonic ($Ma \ll 1$) except for the highest Reynolds numbers. Supersonic flow occurs in the pulse flow experiments in the very coarse (300 μm) GB beds.

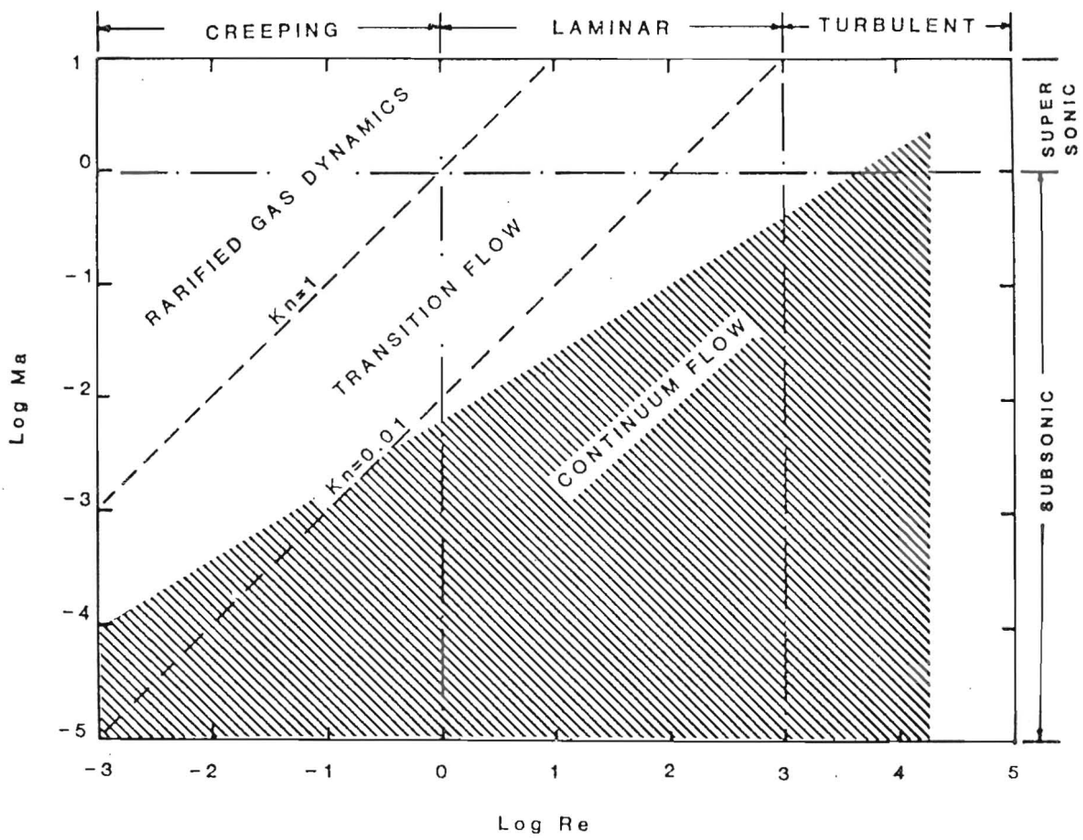

Figure 10: Flow regimes for an ideal gas as a function of Mach number Ma and Reynolds number Re. Lines of constant Knudsen number Kn are also shown. The regime studied in the present experiments is shown as the shaded area.

Quasi–Steady Assumption

The data reduction for the QSS method is based on the steady–state version of Eqs. 1 and 2, *i.e.*, the time derivative term in Eq. 1 is neglected. We will now derive the conditions under which this is possible. For isothermal flows, gas density is directly proportional to pressure and Eq. 1 can be written

$$\frac{\epsilon}{\rho}\frac{\partial \rho}{\partial t} + \frac{1}{\rho}\frac{\partial \dot{m}}{\partial x} = 0, \tag{13}$$

where we have written $\dot{m} = \rho u$ for the mass flowrate. The first term can be estimated as

$$\frac{\epsilon}{\rho}\frac{\partial \rho}{\partial t} \approx \frac{\epsilon}{P_o}\frac{dP_o}{dt}, \tag{14}$$

where P_o is the reservoir pressure. The second term can be estimated as

$$\frac{1}{\rho}\frac{\partial \dot{m}}{\partial x} \approx \frac{1}{\rho_o}\frac{\dot{m}}{L}, \tag{15}$$

where L is the length of the bed. In terms of these estimates, the steady–state criterion is that

$$\frac{\epsilon}{P_o}\frac{dP_o}{dt} \ll \frac{1}{\rho_o}\frac{\dot{m}}{L}. \tag{16}$$

Further reduction of this equation can be performed using the mass flowrate estimated by the solution to the steady flow equations. Substituting the mass flowrate from Eq. 23 below, the steady–state criterion reduces to

$$\epsilon LA \ll V, \tag{17}$$

where A is the bed cross–sectional area. The physical interpretation is that the packed–bed pore volume ϵLA must be much less than the reservoir volume V for the quasi–steady flow assumption to be valid. This inequality was well satisfied in all cases we studied.

Steady Flow Solution

Steady flow in a porous material is generally governed by the steady flow continuity equation and the force balance between drag and pressure drop

$$\frac{\partial \rho u}{\partial x} = 0, \tag{18}$$

$$-\frac{\partial p}{\partial x} = \frac{\rho u^2}{\bar{d}} C_D\left(Re, \epsilon, \bar{d}\right) \tag{19}$$

The solution to the first equation is simply $\dot{m} = \rho u$ = constant, *i.e.*, the mass flux through the bed is independent of position. This implies that the Reynolds number is also independent of position, $Re = \rho u \bar{d}/\mu$ = constant. Together, these two results allow us to rewrite the force balance as

$$-\rho \frac{\partial p}{\partial x} = \frac{\dot{m}^2}{\bar{d}} C_D = \text{constant}. \tag{20}$$

Using the ideal gas law $p = \rho RT$, this equation can be integrated over the length L of the packed bed to yield

$$P_\circ^2 - P_a^2 = 2RT\dot{m}^2 C_D L/\bar{d}, \tag{21}$$

where P_a is the ambient pressure at the bed exit and $P_\circ$ is the reservoir pressure at the bed entrance. This is the most general form of the solution to the steady flow equations for an ideal gas. At this point in the derivation, the solution is still perfectly general and nothing specific to the quasi–steady assumption has been introduced.

QSS Flowrate

In order to use the results derived in the previous section, the mass flowrate $\dot{m}$ through the bed must be known. In this respect, the present work differs from all others in this field. Usually, an additional piece of apparatus must be introduced in order to determine flowrate. Typically this involves inferring the flowrate from the pressure drop measured across a separately calibrated orifice plate or porous bed. Flowrate measurements are difficult and often are the greatest single source of error in these experiments.

The present experiments circumvent this problem by using the pressure signal and the known reservoir volume to calculate absolute mass flowrates. A reservoir of volume V and containing a mass M of gas at pressure $P_\circ$ satisfies the ideal gas law

$$P_\circ V = MRT.$$

If the rate at which mass flows out of the volume is dM/dt and the gas temperature in the reservoir remains constant, then the time derivative of the pressure is

$$\frac{dP_\circ}{dt} = \frac{RT}{V}\frac{dM}{dt}. \tag{22}$$

In the QSS technique, all gas leaving the reservoir flows into the bed so that if the bed cross–sectional area is A, the mass flowrate in the bed is

$$\dot{m} = -\frac{1}{A}\frac{dM}{dt} = -\frac{1}{RT}\frac{V}{A}\frac{dP_\circ}{dt}. \tag{23}$$

In order to use this expression to compute flowrates, the absolute volume of the reservoir must be known and the time derivative of the reservoir pressure computed.

There exist very accurate pressure-volume techniques using standard reference volumes and absolute pressure measurements for determining the reservoir volumes. These techniques were used in the present study. The time derivative of the pressure was computed by the data reduction program described below. Very accurate results could be obtained since the pressure data were digitized directly and the original data were used for the computation. The pressure signals could also be carefully calibrated and all of the nonlinearities of the transducer, amplifier and digitizer removed by the calibration function.

Drag Law Parameters

Using the Forchheimer expression for the drag law (and substituting into the general expression for the steady flow solution) together with the QSS expression for the mass flowrate, we obtain:

$$(P_o^2 - P_a^2) = 2L\frac{\mu}{\kappa}\frac{V}{A}\left(-\frac{dP_o}{dt}\right) + \frac{2L}{RT}\frac{\lambda}{\kappa}\left(\frac{V}{A}\right)^2\left(-\frac{dP_o}{dt}\right)^2 \tag{24}$$

The use of this equation to determine the parameters κ and λ is discussed below.

Data Reduction

A schematic of experimental pressure *vs* time data is shown in Fig. 9b. Shown are the background, nonsteady, and quasi-steady flow periods. After subtracting the background level, the derivative of the pressure in the quasi-steady period is taken with respect to time. This is accomplished with a data reduction program that processes the digital data after they have been transferred to one of the SNLA scientific mainframe computers. A polynomial in time is fit to the reciprocal of the data by the least-squares method. The order of the polynomial is chosen to minimize the residual without introducing extraneous wiggles in the derivative. Typically, polynomial of order 5 to 7 was used. Once the fit was complete, the derivative of the pressure was computed by analytically calculating the derivative of the fit and evaluating the resulting expression at each data point.

Reduction to the general form of the drag law $C_D(Re)$ was straightfoward. The QSS mass flowrate was computed from the calculated pressure signal at each data point and the drag coefficient was evaluated from Eq. 21. The Reynolds number for that point was computed using the previously determined mean particle size $\bar{d}$ and the computed viscosity μ. Each data point yields a different value of Re so that a plot of $C_D(Re)$ can be obtained from each experiment. The range of Re covered in each experiment depends on the permeability of the bed and the initial reservoir pressure. The more permeable the bed and the higher the initial pressure, the wider the range of Re that could be obtained. Of course, care has to be taken that the QSS assumption is not violated.

Computation of the parameters in the Forchheimer form of the drag law is more complex. Referring to Eq. 24, we see that it is a quadratic of the form $y = ax + bx^2$ where $y = (P_\circ^2 - P_a^2)$ and $x = -dP_\circ/dt$. Constants a and b are uniquely related to the parameters κ and λ and the various known physical quantities such as V, L, T, etc. In order to determine a and b, an additional curve–fitting procedure was used. Values of x and y were computed by the same program used to compute the pressure derivative and a least–squares curve fit of x to a quadratic in y was performed. The results of that fit were best estimates of a and b; from these values κ and λ were easily computed.

5 QSS Results

Using the analysis and data reduction techniques described above, drag coefficients $C_D(Re)$ and drag law parameters κ and λ were determined for the materials that were investigated. Not all of these quantities were determined for every material. The glass beads were most extensively investigated and both drag coefficients and drag law parameters were obtained. The widest range of Re and the most information on high Reynolds number flow were obtained in those studies.

Explosives were much denser and much more impermeable and all of those studies were in the low Reynolds number regime. For this reason, no information on drag law is directly reported but only the values of κ and their dependence on porosity. Experimental data are compared to previous investigators' correlations for both types of materials. This comparison is of great interest because prior to this investigation, almost no data were available on the porosity-dependence of the permeability of granular explosives.

Before giving the results, there are two remaining areas of experimental concern that need to be addressed. The first is the presence of the metal frit with the GB beds. The frit added an additional flow resistance. Any correction would have to account for the frit and the frit–to–bead interface. Fortunately, these corrections were negligible for long beds. While the effects were noticeable for very short beds, we found that with the large beads (284 to 111 μm), the permeability was independent of L when L was greater than 15 cm. For the smaller beads, this independence was observed at lengths greater than 5 cm.

The second area of concern was possible wall effects such as channeling. These effects were tested by making QSS runs in tubes of different diameters. For the glass beads, diameters of 4 mm and 12.7 mm were used. For CP, the diameters were 2.5 mm and 4 mm. In both cases, the values of κ and κ/λ were the same within the limits of experimental error, indicating that channeling was not important.

Finally, we must note that some caution must be used when interpreting the results of the data reduction process. Depending on the flow regime, either the viscous or the inertial term will usually dominate the momentum equation, and the other term will be negligible. Parameters for the negligible term will be determined with poor accuracy. For example, κ/λ was negligible with the CP samples because of the low Reynolds number and values of this parameter are very uncertain. Conversely, for the GB beds at very high Reynolds numbers, the data for κ become less meaningful. The error associated with the experimental results for the dominant parameters are of the order of $\pm$ 10%.

5.1 Glass Beads

The κ and κ/λ data for the beads are shown in Table 1. There are several noteworthy observations. We found that the pulse 1onditioning step was not necessary for

the 284 μm and 167 μm diameter beads. The effect of the pulse conditioning is shown dramatically with the smaller beads. The run for the 14 μm diameter beads labeled BP is before the pulse conditioning. The same bed after conditioning (AP) shows a significant decrease in ϵ, L, κ, and κ/λ.

The experimental values for κ tend to be consistently higher than predicted. The experimental values of κ/λ seem to be in reasonably good agreement with the predicted values except with the small diameter beads. Here the disagreement is not surprising in view of the flow regime arguments mentioned earlier. For the glass beads, the predicted values were calculated with the constants originally reported in Refs. 1-3.

Figure 11 is a log–log plot of the GB κ data *vs* the mean particle size ($\bar{d}$). Since the porosities of all the GB beds were nearly the same, this is a valid comparison. What this plot reveals is that the trend of the κ data is the same for the experimental data and either porosity correlation. By adjusting McDonald's or Rumpf-Gupte's constants slightly, the experimental data would reasonably fit either correlation.

The drag coefficient *vs* Reynolds number is shown in Fig. 12. In this form, differences in porosity between the individual beds result in separate families of curves. If the data are replotted using MacDonald's variables, $C_D\epsilon^3/(1-\epsilon)$ *vs* $Re_d/(1-\epsilon)$, the differences are diminished.

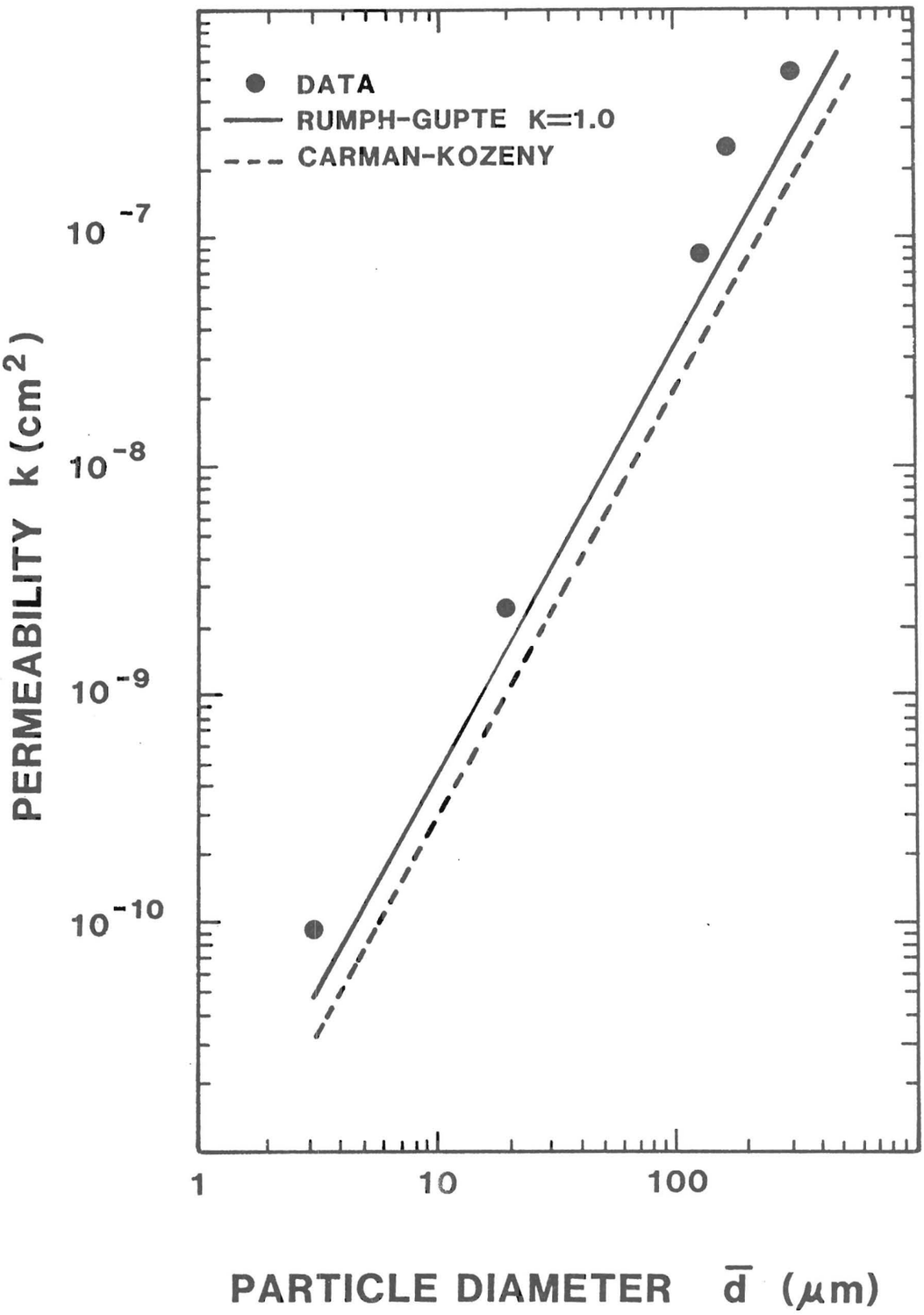

Figure 11: Measured permeability of the glass bead packed beds as a function of surface mean particle diameter. The correlations of Carman-Kozeny and Rumpf-Gupte ($K = 1$) are also shown.

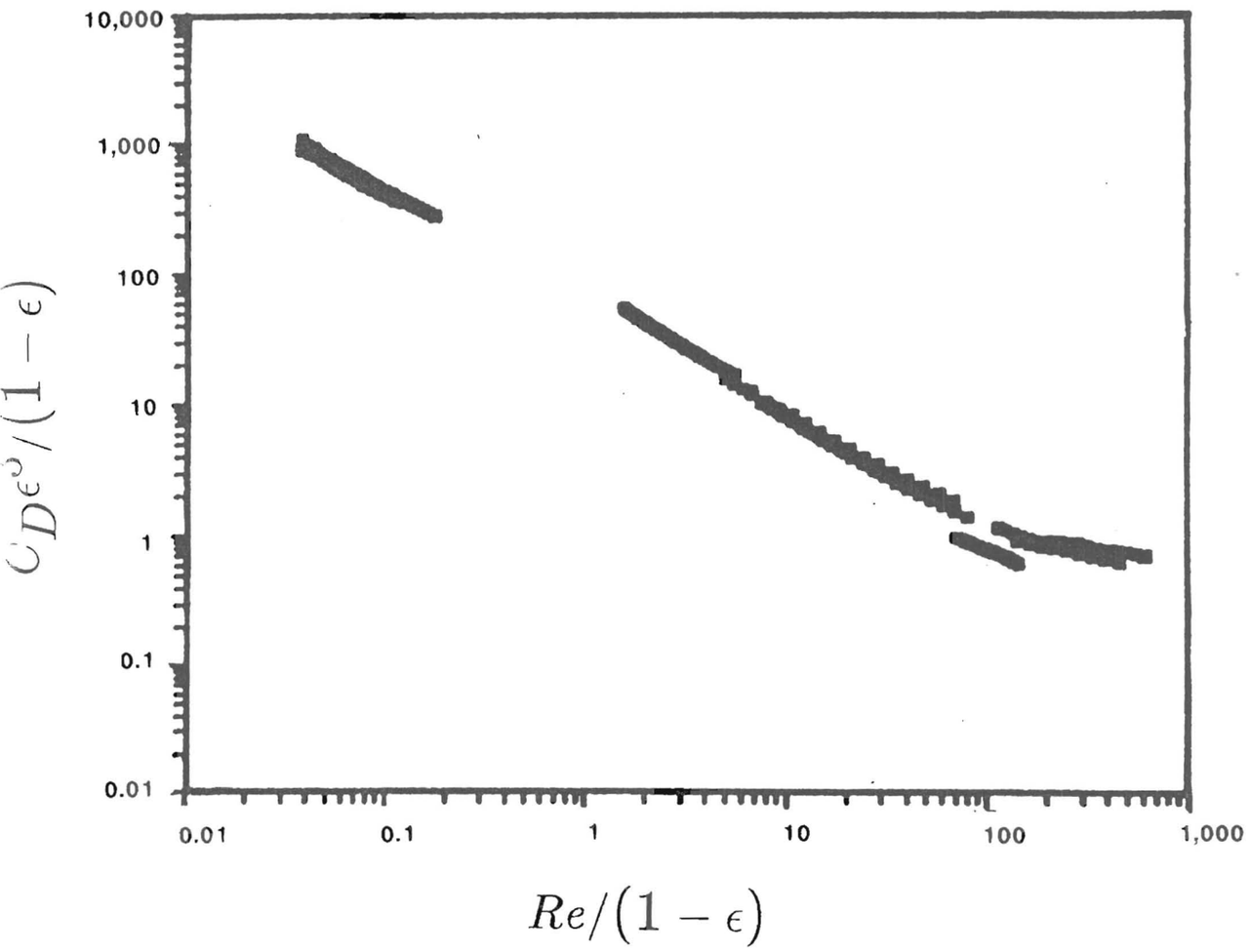

Figure 12: Measured drag coefficient of the glass bead packed beds as a function of the Reynolds number.

5.2 Explosives - CP

The CP results are given in Table 2. Figure 13 shows κ as a function of the porosity for the two lots of CP tested. The dashed lines are the predicted results for Carman-Kozney correlation (uppermost), the solid lines are for Rumpf-Gupte correlation (lower), and the points are the experimental data. The original version of the Carman-Kozeny equation is used

$$\kappa_m = \frac{\bar{d}^2 \epsilon^3}{180(1-\epsilon)^2}$$

with a value of $\bar{d} = 10\mu$m for the EL47344 data and the measured values of $\bar{d}$ (variable) used for the EL41088 data. The constant K in the Rumpf and Gupte correlation

$$\kappa_{rg} = \frac{\bar{d}^2 \epsilon^{5.5}}{5.6K}$$

was adjusted to yield the best fit with the data. For lot EL41088, $K = 5.6$ was used in Fig. 13 and for lot EL47344, $K = 39$. This adjustment procedure results in the better fit for the Rumpf-Gupte correlation. Unfortunately, there is no theory for predicting the value of K, which apparently depends both on the material type and preparation.

Even if the constant in the Carman-Kozney equation is adjusted to best fit the data shown in Fig. 13, it appears that for permeabilities below 10^{-11} cm^2, the porosity dependence is closer to $\epsilon^{5.5}$ than $\epsilon^3/(1-\epsilon)^2$. When κ is greater than 10^{-11} cm^2, either correlation is satisfactory.

We conclude that for very nonideal porous materials such as CP, the permeability must be measured experimentally and that correlations based on spherical particles should be used very cautiously. The Carman-Kozeny relation overestimates κ by a factor of 10-55 for CP; the original Rumpf-Gupte correlation overpredicts κ by a factor of 5.6-39.

Apparently, both correlations fail because the mean *particle* size is such a poor predicitor of the mean *pore* size in these nonideal (nonspherical) porous materials such as compacted granular explosives. It is not obvious why the Rumpf-Gupte porosity dependence is followed for CP since both the particle size and porosity are simultaneously changing during compaction.

The observed variation of permeability with compaction suggests that as the porosity decreases ($\epsilon \rightarrow 0$), the permeability becomes independent of initial particle size and consequently becomes a function of the porosity only. For unconsolidated or loosely packed materials, the initial particle size will dominate the distribution and a correlation similar to Rumpf-Gupte (corrected for the nonspherical pores) should be appropriate.

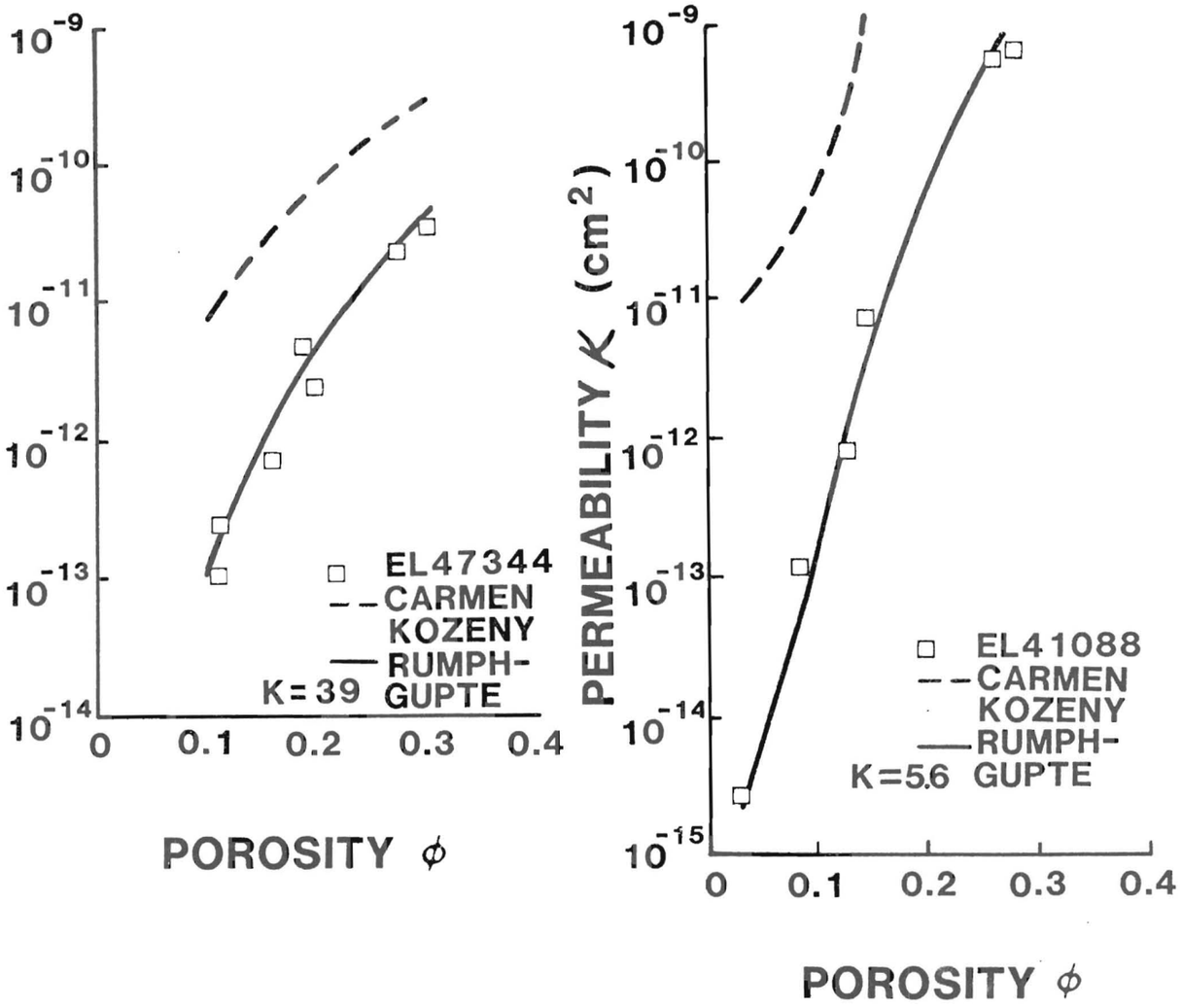

Figure 13: Measured permeability of two lots of CP packed beds as a function of porosity. The correlations of Carman-Kozeny and Rumpf-Gupte are also shown.

5.3 Explosives - HMX

The HMX data are given in Table 3 and the permeability as a function of porosity is given in Figure 14. No comparison with the correlations is given since no particle size measurements were made. The values of κ were 5-10 times larger than those measured for CP at the same porosity. These values are consistent with particle sizes of 30-50 μm.

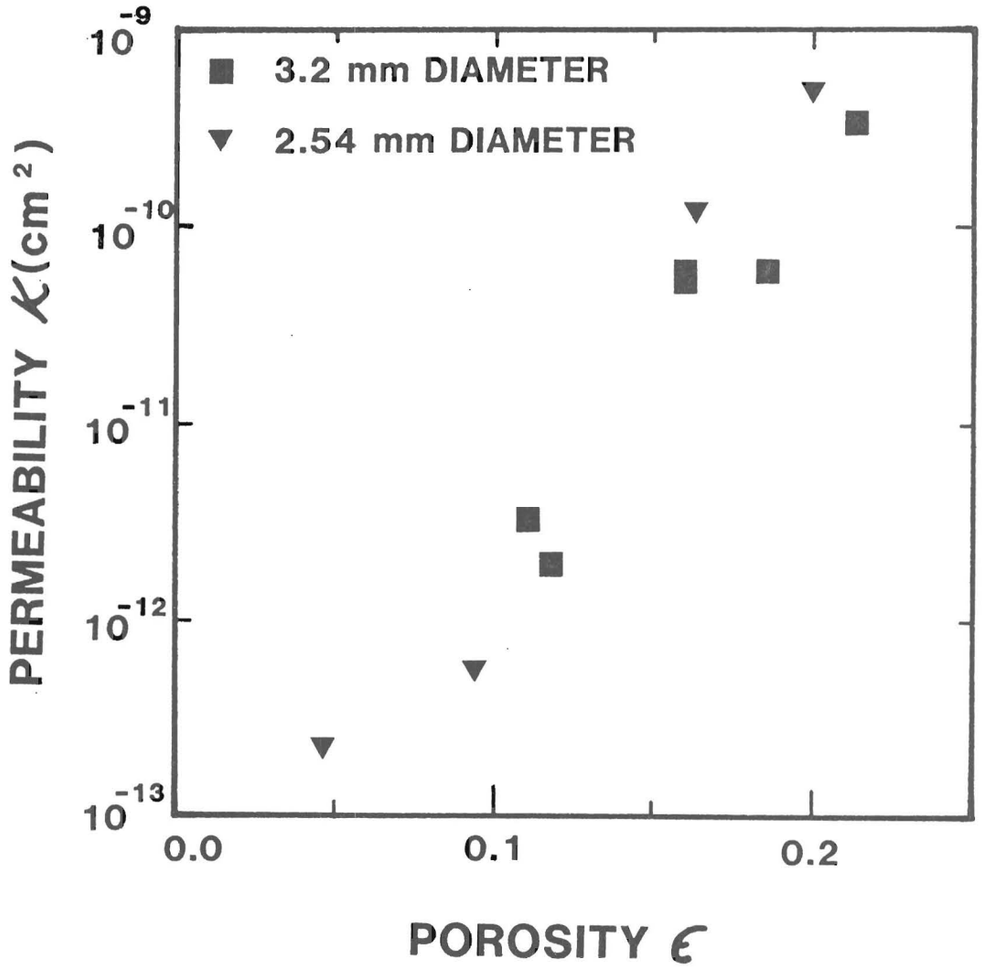

Figure 14: Measured permeability of HMX packed beds as a function of porosity.

5.4 Explosives - HNS

The HNS data are given in Table 4 and the permeability as a function of porosity is given in Figure 15. No comparison with the correlations is given since particle size measurements were not made. As a rough guideline, the mean particle size of the Type I grains is between 5 to 10 μm and Type IIa grains are about twice as large. The κ values for Types I and IIa are reasonably consistent with CP at the same porosity. The particle size of hyperfine (HF) HNS is about 1 to 2 μm. The low value of κ ($< 10^{-13}$) at a porosity of 0.2 for the HF HNS reinforces our conclusion that the permeability of these nonideal porous materials must be measured experimentally.

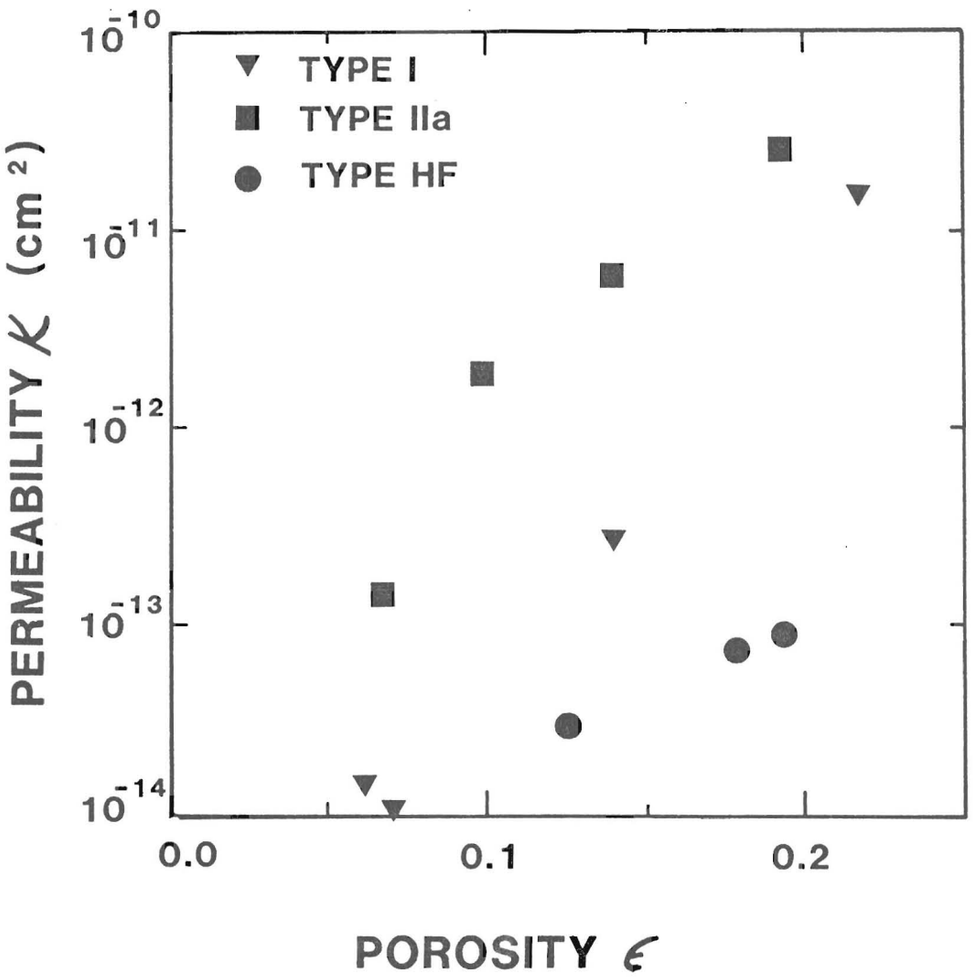

Figure 15: Measured permeability of HNS packed beds as a function of porosity.

6 Transient Pulse Experiments

6.1 Apparatus and Technique

This method is relatively simple to set up and perform; however, the mathematical model of the flow is more complex. For this reason, the results are not as useful in obtaining quantitative data on permeability as are those of the QSS technique. The method does illustrate some interesting features of transient compressible flow in porous materials that may be applicable to combustion problems such as DDT.

The basis of the technique is to apply a step–function pressure pulse to the front of the bed, and then to observe the propagation of the pulse through the bed. We have used beds with a closed end for experimental reasons; a convenient place for observing the pulse is at the end of the bed. A pressure gauge was used to constrain the bed in the initial preparation as described earlier. In some cases, we also installed pressure gauges along the sides of the beds.

A schematic of the apparatus was shown in Fig. 8. The gauge to monitor the input pulse is designated P_0 and P_1 to P_4 monitor the pulse as it travels through the bed. These gauges are either piezoelectric or semiconductor type for fast response to high–pressure signals. The step-function input gas pulse is obtained by miniature shock tube arrangement.

The reservoir V_1 is charged to a pressure just below the burst pressure of the rupture disc D. A pneumatically controlled valve separates volumes V_1 and V_2. This valve is then closed and V_2 is charged to a higher pressure so that when the separation valve is actuated, the new pressure in the combined volumes exceeds the burst pressure of the rupture disc. A shock wave is produced when the disc ruptures. The wave travels down the plumbing and reflects from the front of the packed bed. After several reverberations of the shock within the plumbing system, the gas pressure on the front of the bed settles down to a constant value. This produces a pressure pulse that for all practical purposes is a step–function. A typical example of the traces obtained (P_0 through P_4) is shown in Fig. 16. The entire system is constructed of commercially available high–pressure hardware, and is capable of producing pulses from 200 to 30,000 psi. The rupture discs are also commercially available; however, for small pressure pulses, it was more convenient to use discs of aluminum and simply form the rupture disc in place. After a run, it was imperative that the system was bled down to ambient pressure slowly to avoid disturbing the porous bed.

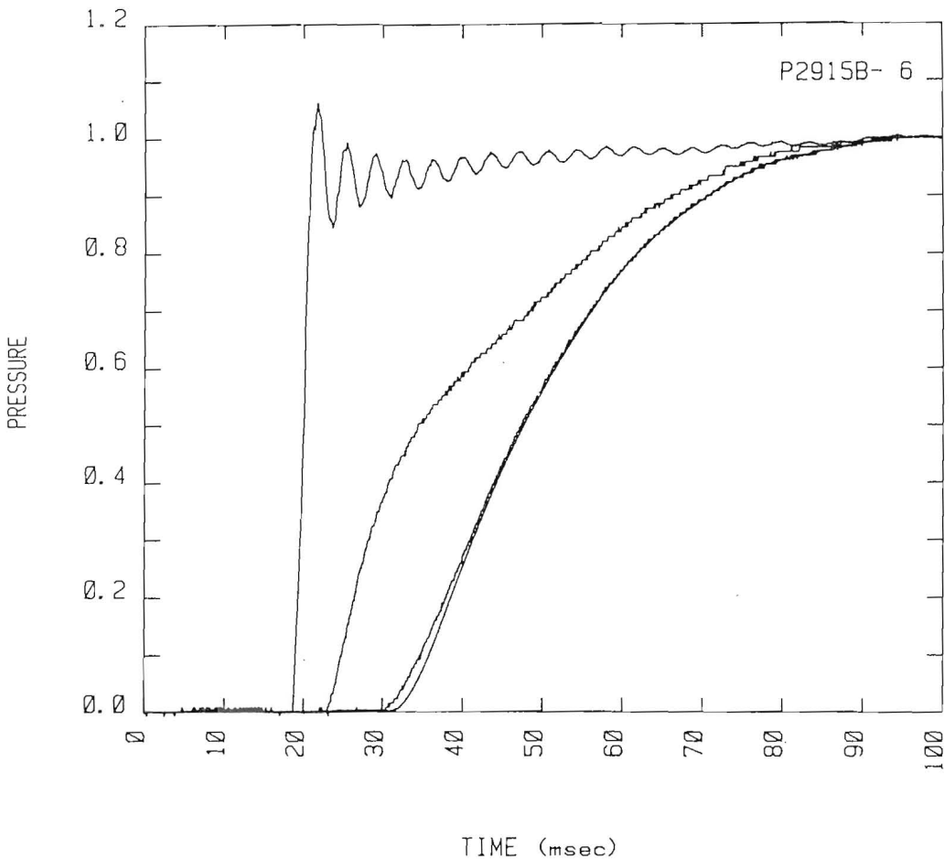

Figure 16: Typical pressure signals from the transient gas pulse experiment.

6.2 Analysis

The basis for analyzing the transient problem is Eqs. 1 and 2. This has been carried out by Morrison[8-10] and Nilson[11] for several cases. We have reanalyzed the problem to obtain results that are more relevant to the present configuration. Numerical solutions to the complete set of equations are given for selected cases corresponding to the GB experiments. Analytical solutions are obtained to both the high and low Reynolds number approximations to the drag law. A simple integral analysis is used to develop an approximate solution for the entire range of Reynolds numbers.

Before discussing the solutions, dimensional analysis will be used to find the scaling parameters and nondimensional variables. The characteristic pressure in the problem is $\Delta P = P_o - P_a$; where P_o is the reservoir pressure and P_a is the ambient pressure level in the bed prior to the test. The characteristic length scale will be chosen to be the packed bed length L. At this point, the characteristic velocity scale U is undetermined. The characteristic time scale $T = \epsilon L/U$ will be determined once the scaling velocity U is chosen. Scaled variables are

$$\Pi = \frac{p - P_a}{\Delta P}, \quad \tau = \frac{t}{T}, \quad \chi = \frac{x}{L}, \quad \mathcal{U} = \frac{u}{U} \tag{25}$$

Note that the scaled density is identical to the scaled pressure for isothermal flows. Scaled versions of Eqs. 1 and 2 are

$$\frac{\partial \Pi}{\partial \tau} + \frac{\partial}{\partial \chi}\left[(\Pi + \delta)\,\mathcal{U}\right] = 0. \tag{26}$$

and

$$-\frac{\partial \Pi}{\partial \chi} = \left(\frac{UL\alpha\mu}{\Delta P}\right)\mathcal{U} + \left(\frac{U^2 L\beta}{RT}\right)(\Pi + \delta)\,\mathcal{U}^2, \tag{27}$$

where the parameter δ is related to the overpressure ratio $N = P_o/P_a$ by

$$\delta = \frac{1}{N-1} \quad . \tag{28}$$

For an idealized shock tube problem, the initial conditions are that the pressure in the bed is at ambient, therefore $\Pi = 0$. The boundary condition at the reservoir end is

$$\Pi = 1 \quad \text{at} \quad \chi = 0 \quad . \tag{29}$$

At the opposite end (exit), the bed can be either opened or closed. If the bed is open, the boundary condition is simply that the pressure is fixed at the atmospheric value,

$$\Pi = 0 \quad \text{at} \quad \chi = 1 \quad . \tag{30}$$

If the bed is closed, the boundary condition (from the drag law) is

$$\frac{\partial \Pi}{\partial \chi} = 0 \quad \text{at} \quad \chi = L. \tag{31}$$

Note that boundary conditions on the velocity have not been derived. These are not needed since it is possible to eliminate velocity entirely and reduce the problem to a single nonlinear equation for the pressure. Before this is done there are two further simplifications that can be made to the equations. First, the problems of interest to us correspond to small values of the parameter δ, *i.e.*, large values of the reservoir pressure $P_\circ$. In what follows, we will take the limiting case of that approximation, $\delta = 0$. Second, there remain two rather ugly looking dimensionless parameters in the drag law since the velocity scale has not been fixed. There are two ways in which the velocity scale can be chosen to beautify the equations and reduce the number of parameters to one. These two choices are both important and are appropriate to either low or high Reynolds number flows. Each possibility is discussed separately below.

6.2.1 Low Reynolds Number Scaling

The coefficient of the first term in the drag law can be set equal to unity if the velocity scale is chosen to be

$$U = \frac{\kappa \Delta P}{\mu L}$$

A physical interpretation of this velocity is that it is the value obtained by using the scaling parameters to estimate the Darcy (low Reynolds number) term in the drag law. The remaining parameter in the drag law is the coefficient of the second term in the drag law. We will denote this term by $\mathcal{R}$ to suggest the resemblence to a Reynolds number defined by the scaling parameters

$$\mathcal{R} = \frac{U\lambda}{\nu_\circ} = \frac{\kappa \Delta P}{\mu L}\lambda \frac{\Delta \rho}{\mu} \tag{32}$$

where we have substituted the permeability $\kappa = 1/\alpha$ and Forchheimer constant $\lambda = \beta/\alpha$ and have defined the characteristic viscosity as $\nu_\circ = \mu/\Delta\rho$. Morrison[10] first used this parameter to characterize transient flows in finite length beds.

The resulting nondimensional versions of Eqs. 1 and 2 are (in the limit $\delta \to 0$)

$$\frac{\partial \Pi}{\partial \tau} + \frac{\partial}{\partial \chi}(\Pi \mathcal{U}) = 0 \tag{33}$$

and

$$-\frac{\partial \Pi}{\partial \chi} = \mathcal{U} + \mathcal{R}\Pi\mathcal{U}^2 \tag{34}$$

The drag law, Eq. 34, can be easily used to eliminate velocity as a variable and obtain a single equation for pressure. In the extreme limit of $\mathcal{R} \to 0$, this equation simplifies to

$$\frac{\partial \Pi}{\partial \tau} = \frac{\partial}{\partial \chi}\left(\Pi \frac{\partial \Pi}{\partial \chi}\right) \tag{35}$$

This equation and the more general version for finite pressure ratio N but zero $\mathcal{R}$ have been considered by Morrison.[8] He obtained numerical solutions for the shock tube problem in finite length beds and demonstrated that a self–similar solution exists for the shock tube problem on a semi–infinite domain.

Equation 35 has the form of the heat equation for a material whose thermal conductivity is proportional to temperature. Like the heat equation, the solutions are diffusive and a disturbance will spread like $\sqrt{t}$. However, one important difference from the heat equation is that the fastest disturbances move at a finite rather than an infinite speed. In terms of the heat equation analogy, this is due to the thermal conductivity vanishing as the strength of the disturbance vanishes.

We have solved the more general model of Eqs. 33 and 34 numerically by using the method–of–lines (MOL) program published by Hyman.[12] For R = 0, *i.e.*, the case corresponding to Eq. 35, the solutions for Π *vs* χ and τ are shown in Figs. 17 and 18. From our results and the analytical and numerical results of previous workers, the following features of the shock–tube solutions can be deduced.

The step–function increase in pressure at the beginning of the packed bed produces a pressure wave of finite extent that spreads into the bed. The pressure Π in the wave monotonically decreases from the reservoir pressure to zero at the head of the wave. The location of the head of the wave $\ell(t)$ moves in a diffusive manner, $\ell(t) \sim \sqrt{t}$. The presence of the end of the packed bed does not influence bed motion until the head of the wave reaches the end of the bed.

We can take advantage of the finite rate of propagation for the wave head to compute the transit time of the pulse through the packed bed. If the pressure pulse is applied at time zero, then the transit time is equal to the time of arrival of the first pressure disturbance at the end of the bed. Until this time, the similarity solution discussed by Morrison[8] and Nilson[11] for Eq. 35 is valid. The solution is a function only of the similarity variable

$$\theta = \frac{\chi}{\sqrt{\tau}} \tag{36}$$

and N for $\mathcal{R} \to 0$. This implies that the wave head location is given by a value of the similarity variable, denoted θ^*, that depends only on the nondimensional parameter N. Morrison's results[8] indicate that for the limiting case of $N \to \infty$, the wave head is located at $\theta^* \approx 1.62$.

In terms of the physical variables, the time t_d at which the head of the wave arrives at the end of the bed ($\chi = 1$) is

$$t_d = 0.381 \frac{\epsilon \mu L^2}{\kappa \Delta P}. \tag{37}$$

This equation can be generalized to the cases with finite N and nonzero $\mathcal{R}$ by observing that the numerical solutions of the full equations must yield the scaled time of pulse arrival at the end of the bed τ^* as a function of the parameters N and $\mathcal{R}$ only. A generalized pulse transit time correlation must then have the form

$$t_d = \frac{\epsilon \mu L^2}{\kappa \Delta P} f\left(N, \mathcal{R}\right). \tag{38}$$

Numerical solutions of Eqs. 33 and 34 must be used to determine the function f. We have done this for the limit $N \to 0$ and finite $\mathcal{R}$; from the similarity solution results we know that $f \to 0.381$ as $\mathcal{R} \to 0$. The general results are discussed below.

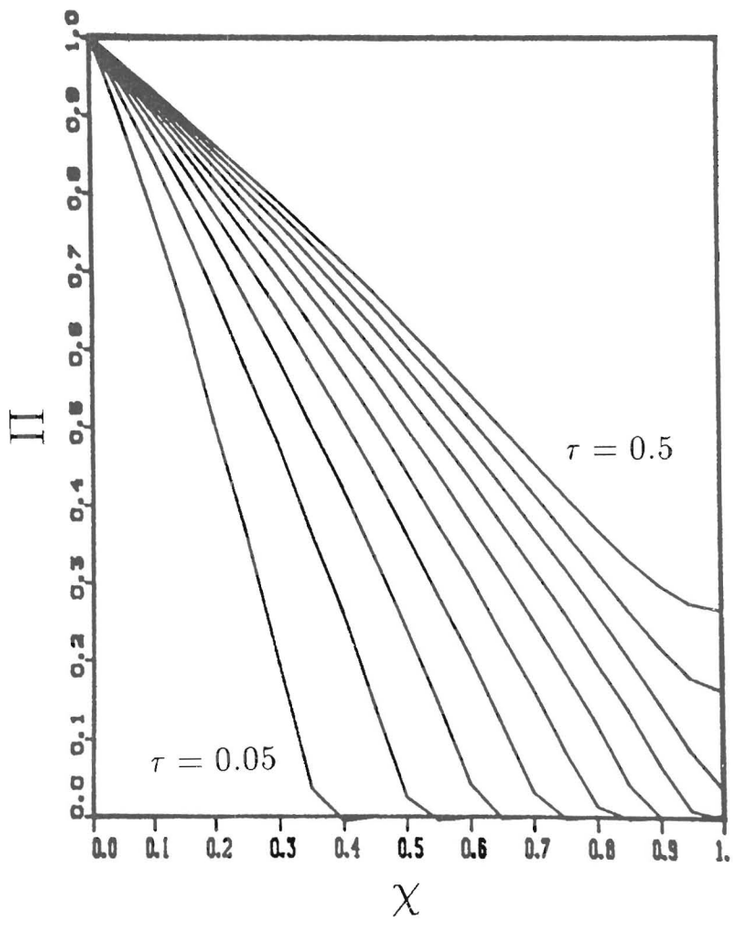

Figure 17: Numerical solution to Eq. 35 ($\mathcal{R} = 0.01$ and $\delta = 0$) by method of lines. Shock tube boundary conditions on a finite domain with a closed end. Nondimensional pressure Π *vs* distance χ for selected times $\tau = 0.05, 0.1, \ldots, 0.5$.

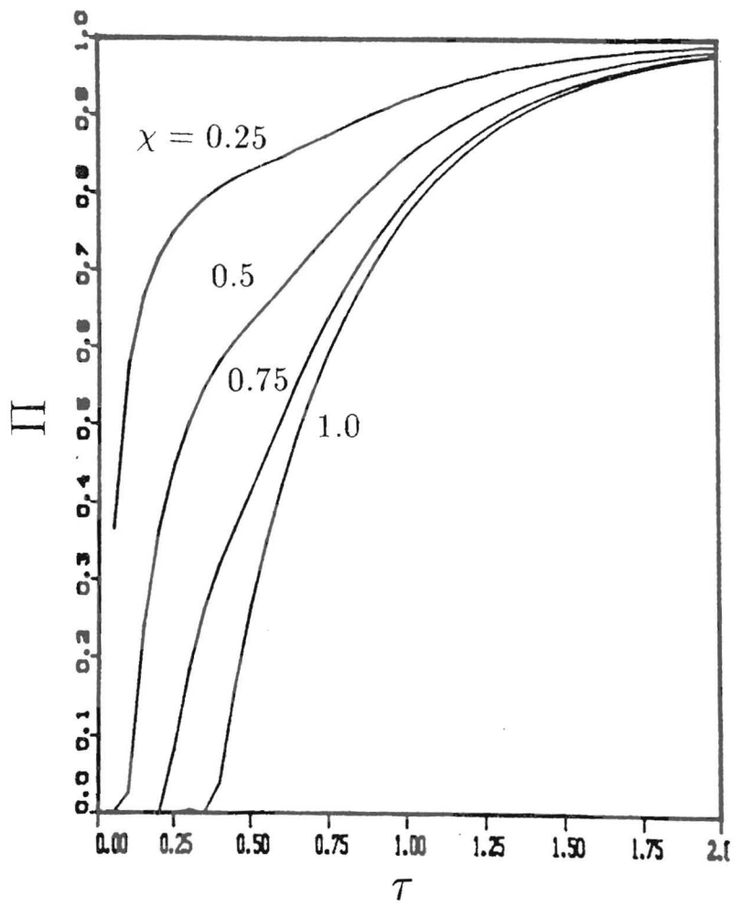

Figure 18: Numerical solution to Eq. 35 ($\mathcal{R} = 0.01$ and $\delta = 0$) by method of lines. Shock tube boundary conditions on a finite domain with a closed end. Nondimensional pressure Π *vs* time τ at selected locations χ (= 0.25, 0.5, 0.75, 1.0) within the bed.

6.2.2 High Reynolds Number Scaling

The coefficient of the second term in the drag law can be set equal to unity if the velocity scale is chosen to be

$$U = \sqrt{\frac{\kappa RT}{\lambda L}}$$

A physical interpretation of this velocity is that it is the value obtained by using the scaling parameters to estimate the Ergun (high Reynolds number) term in the drag law. The remaining term in the drag law can be expressed in terms of the parameter $\mathcal{R}$ defined above. The nondimensional version of Eq. 1, the continuity equation, is the same as Eq. 33 derived above. The nondimensional version of Eq. 2, the drag law, is (in the limit $\delta \to 0$)

$$-\frac{\partial \Pi}{\partial \chi} = \frac{\mathcal{U}}{\sqrt{\mathcal{R}}} + \Pi \mathcal{U}^2 \tag{39}$$

As in the low Reynolds number case, the drag law (Eq. 39) can be used to eliminate velocity as a variable and obtain a single equation for pressure. In the extreme limit of $\mathcal{R} \to \infty$, that equation simplifies to

$$\frac{\partial \Pi}{\partial \tau} = -\frac{\partial}{\partial \chi}\left(-\Pi \frac{\partial \Pi}{\partial \chi}\right)^{1/2} \tag{40}$$

This equation and the more general version for finite pressure ratio N and infinite $\mathcal{R}$ has been considered by Morrison.[9,10] He obtained numerical solutions for the shock tube problem in finite length beds and demonstrated that a self–similar solution exists for the shock tube problem on a semi–infinite domain.

Solutions to Eq. 40 for the shock tube problem are very similar in character to those of Eq. 35, the low Reynolds number analog discussed above. Because of the square root term, the motion of the wave head follows a different power law, $\ell \sim t^{2/3}$. Numerical solutions to Eq. 40 are shown in Figs. 19 and 20. These solutions were obtained by the same MOL program used for the low Reynolds number cases discussed above. Solutions for similar cases but with the end of the bed open to the atmosphere are given by Morrison.[10]

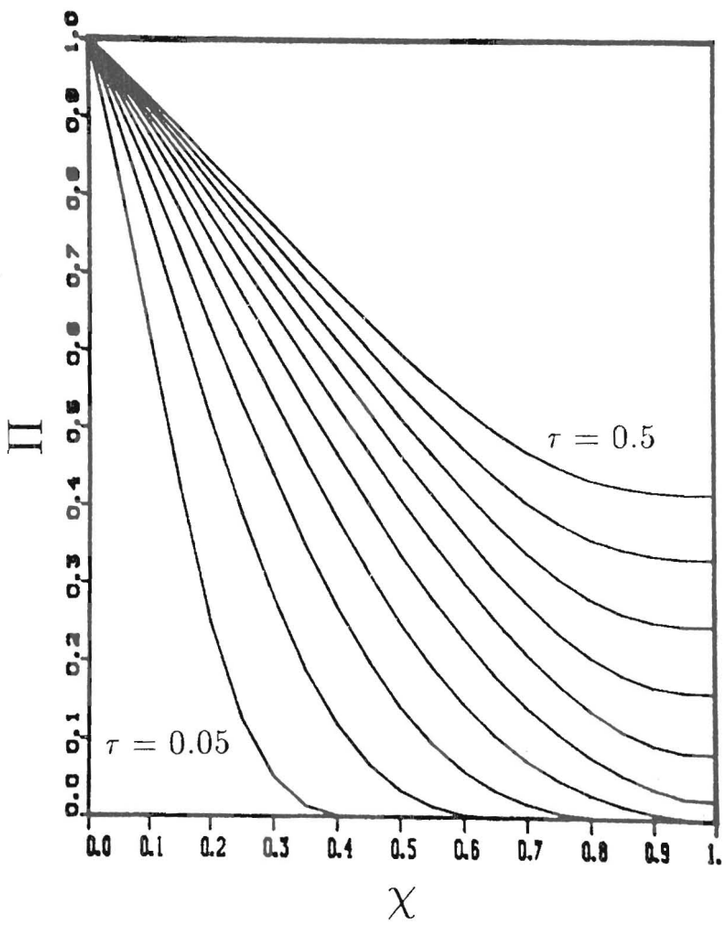

Figure 19: Numerical solution to Eq. 40 ($\mathcal{R} = 10^3$ and $\delta = 0$) by method of lines. Shock tube boundary conditions on a finite domain with a closed end. Nondimensional pressure Π *vs* distance χ for selected times $\tau = 0.05, 0.1, \ldots, 0.5$.

As in the low Reynolds number case, the pulse transit time through the bed can be estimated using the similarity solution derived for the semi–infinite domain. In the present case, the similarity variable θ is

$$\theta = \frac{\chi}{\tau^{2/3}} \tag{41}$$

Morrison's numerical results[9] indicate that the wave head is located at $\theta^* \sim 3$ in the limit $N \to \infty$. Due to the slightly different structure of the equations, the wave head is not as well defined in the high Reynolds number case as in the low Reynolds number case.

In terms of the physical variables, the time t_d at which the head of the wave (the first pressure signal) arrives at the end of the bed ($\chi = 1$) is

$$t_d = 0.19\epsilon L^{3/2}\sqrt{\frac{\lambda}{RT\kappa}}. \tag{42}$$

Unlike the analogous low Reynolds number expression, this time is *independent* of the overpressure. Like the low Reynolds number case, this result can be generalized for finite N and $\mathcal{R}$ to construct a transit time function

$$t_d = \epsilon L^{3/2}\sqrt{\frac{\lambda}{RT\kappa}}g\left(N, \mathcal{R}\right) \tag{43}$$

from numerical solutions of Eqs. 33 and 39. This has been done for a number of cases in the limit $N \to 0$ and is discussed below.

6.3 Results

To summarize, the principal results of the analysis are the development of scaling parameters, nondimensional equations and numerical solutions for the shock tube problem. A "pseudo" Reynolds number $\mathcal{R}$ can be defined

$$\mathcal{R} = \frac{U\lambda}{\nu_\circ} = \frac{\kappa\Delta P}{\mu L}\lambda\frac{\Delta\rho}{\mu} \tag{44}$$

and used to completely characterize the flow regimes for the shock tube problem. At the extremes of the flow regimes, similarity solutions can be used to estimate the pulse transit time t_d. We have compared both the detailed numerical solutions and transit time data with the results of nitrogen pulse experiments in glass bead packed beds. Experiments were performed over a wide range of values of $\mathcal{R}$ to provide a thorough test of the theoretical ideas. The results of these comparisons are discussed below.

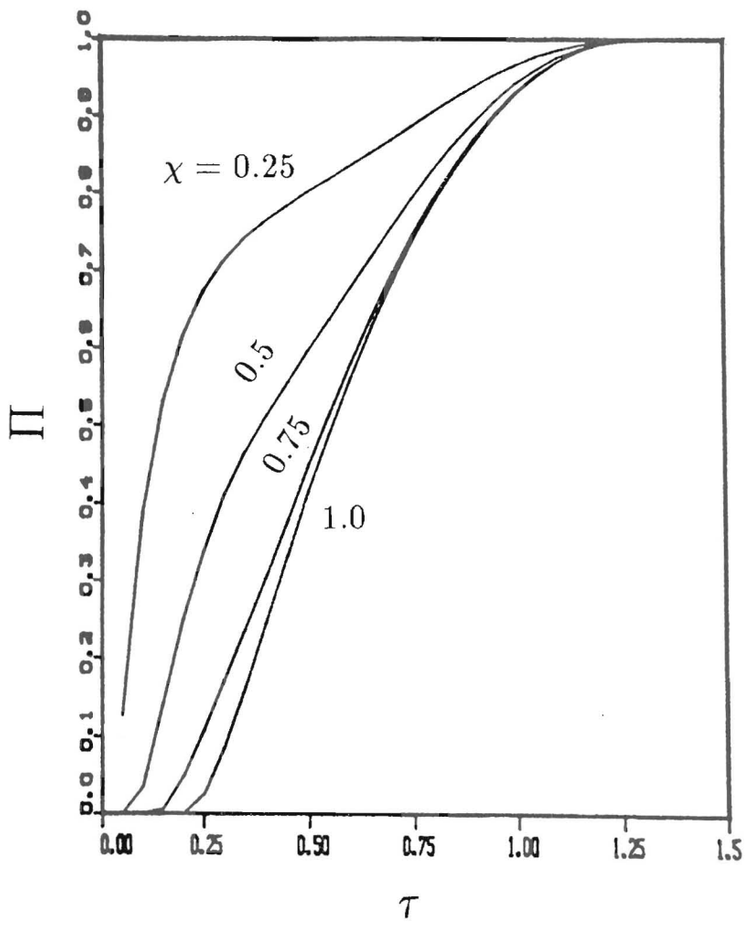

Figure 20: Numerical solution to Eq. 40 ($\mathcal{R} = 10^3$ and δ =0) by method of lines. Shock tube boundary conditions on a finite domain with a closed end. Nondimensional pressure Π *vs* time τ at selected locations χ (= 0.25, 0.5, 0.75, 1.0) within the bed.

6.3.1 Transit Time

The transit time formulas take particularly simple forms in the limit of $N \rightarrow \infty$. In practical terms, the asymptotic results are valid for $N \geq 40$. These results, given above but repeated here for completeness, are

$$t_d = 0.381 \frac{\epsilon \mu L^2}{\kappa \Delta p} \quad \text{for} \quad \mathcal{R} \leq .01, \tag{45}$$

$$t_d = 0.19 \epsilon L^{3/2} \sqrt{\frac{\lambda}{RT\kappa}} \quad \text{for} \quad \mathcal{R} \geq 10. \tag{46}$$

For intermediate values of $\mathcal{R}$, *i.e.*, for $.01 \leq \mathcal{R} \leq 10$, the relationship $\tau^*(\mathcal{R})$ must be determined numerically. Results for both low and high Reynolds number scaling are given in Fig. 21. Note the large increase in the value of τ^* for increasing (decreasing) $\mathcal{R}$ for low (high) Reynolds number scaling. At $\mathcal{R} = 1$, the scaled equations are identical for both scaling methods and the values of the scaled transit times are identical. Decreasing N below 50 results in increasing values of τ^* (longer transit time) for either type of scaling.

Experimentally, transit times were determined by examining the digital records of the pressure signals and subtracting the arrival time at P_4 from the arrival time at P_0. This was reasonably accurate since the arrival time was usually quite distinct and the transit time was much larger than the initial pulse rise time. Data from experiments over a wide range of reservoir pressures and bead sizes are shown in Fig. 22.

Generally, the data from beds formed with small diameter beads were in the low Reynolds number regime; large diameter beads resulted in high Reynolds number regime data. In the plot, this difference is reflected in the pressure dependence of the data. The 10 μm bead beds show an inverse pressure dependence in accord with the low Reynolds number scaling. The 300 μm beads show a pressure independence in accord with the high Reynolds number scaling. The intermediate curves reflect the transitional behavior of those cases.

Transit time data can also be used to infer the values of the permeability and Forchheimer constant. Values obtained in this fashion agree reasonably well with those independently obtained by the QSS method. Uncertainty estimates suggest that much larger error bounds should be assigned to the values determined by the pulse method than from the QSS technique. It is possible to obtain much higher values of the Reynolds number in the pulse than in the QSS experiment. This constitutes the principal advantage of the pulse method for quantitative measurements. Unfortunately, this advantage cannot be realized with many reacting materials since the pressure pulse will often cause ignition.

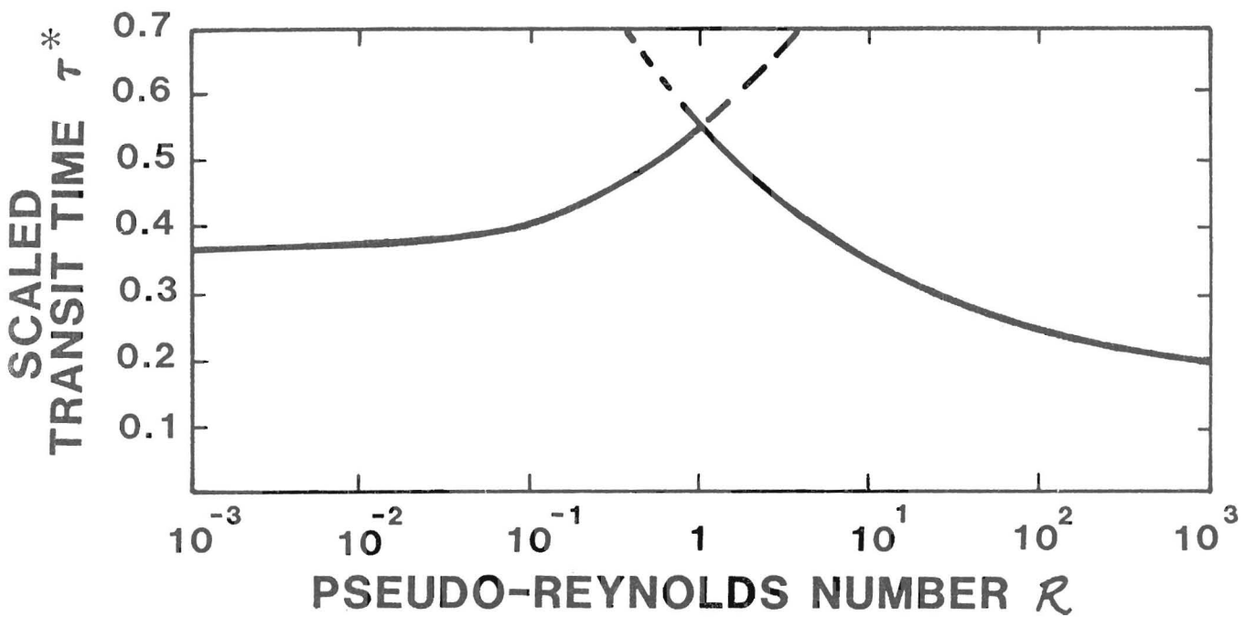

Figure 21: Scaled transit times τ^* *vs* "pseudo" Reynolds number $\mathcal{R}$. Both low and high Reynolds number scaling are shown as indicated. Results obtained by numerical (MOL) solution of the scaled equations for $N = \infty$.

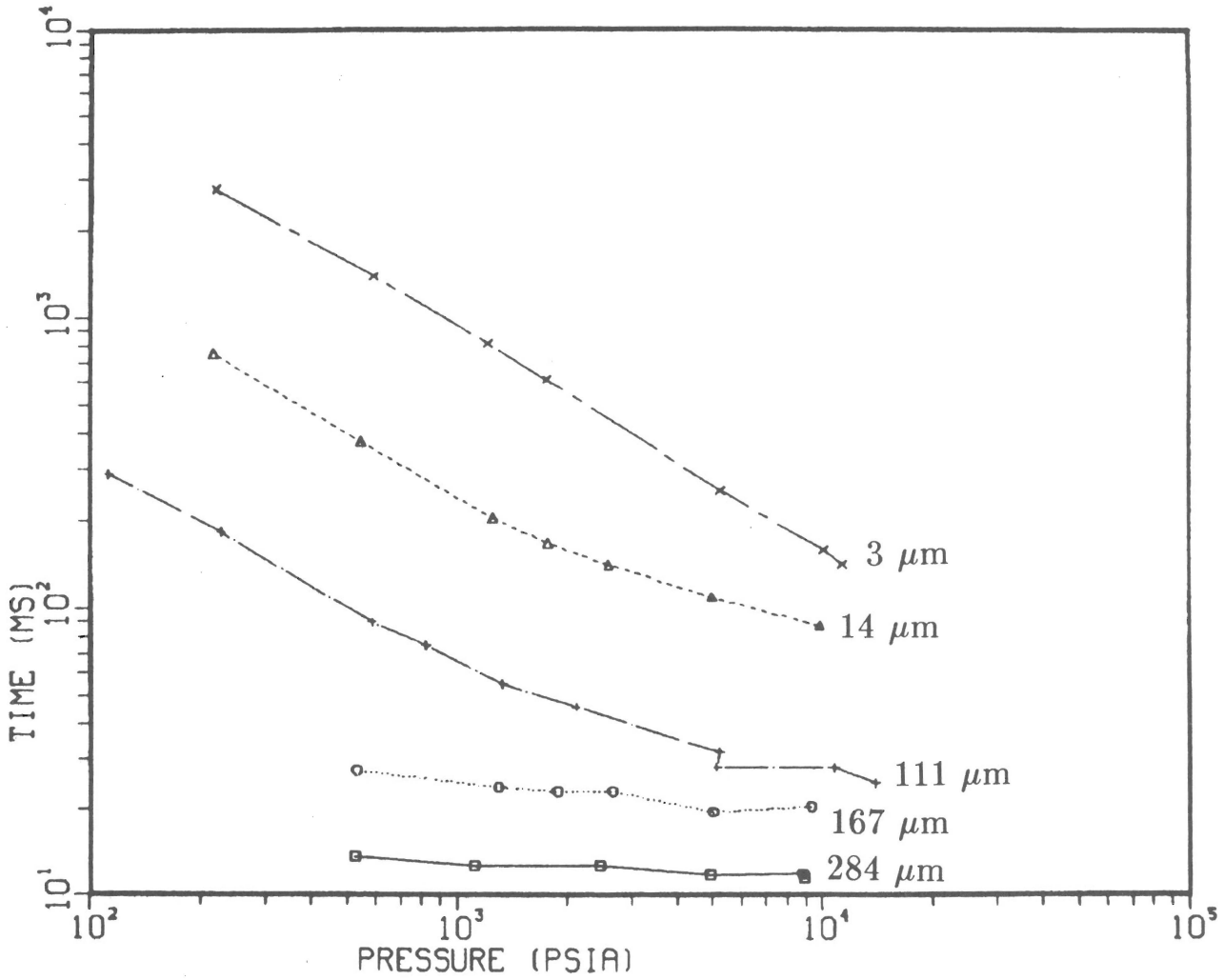

Figure 22: Experimental transit times t_d *vs* driving pressure ΔP. Data from glass bead packed beds.

6.3.2 Pressure Signals

For a few selected experiments, measured pressure signals were compared with detailed numerical results. Pressure was computed as a function of time for selected locations corresponding to the center of the pressure transducer in the experiments. Comparisons are shown below for two cases.

The first case is a low Reynolds number experiment performed with a packed bed of calcium chromate ($CaCrO_4$). This material was used in preliminary experiments not described in this report. Calcium chromate is a granular inert material that is used to simulate pyrotechnics. The effective particle size was 1.4 μm if the Karman-Cozeny formula is used to match the measured permeability. The bed porosity was 0.25 and pressure transducers were located at 0, 1.15, 3.69, and 4.96 cm from the entrance to the bed. A driving pressure of 155 psia was used in the experiment. A value of $\mathcal{R} = 10^{-4}$ was used in the MOL simulation.

Results of the experiment and simulation are shown in Fig. 23. Note that normalized pressure is plotted against actual time for both experiment and computation. The initial spike observed in pressure signal 1 is due to the transient processes that occur when the rupture disk breaks. After the shock waves are attenuated, the pressure remains at essentially a constant level. A low resolution (8-bit) digitizer was used for recording these data and single–bit noise is visible on all traces. Comparison with the simulation results indicates that the observed shape of the waveform is very well reproduced.

The second case is an intermediate Reynolds number experiment performed with the 10 μm glass bead packed bed that was described earlier in this report. The driving pressure was 4900 psia and pressure transducers were located at 0, 2.68, 5.22, and 5.83 cm. Since the signals from the last two transducers were almost indistinguishable, only the transducer at 5.83 cm was modeled in the numerical simulation. A value of $\mathcal{R} = 2$ was used in the simulation.

Results of the experiment and simulation are shown in Fig. 24. The oscillations in pressure due to the shock wave reverberations are now plainly visible in pressure signal 1. Due to the tremendous drag forces on the gas in the bed, these oscillations will be rapidly damped and no effect on the interior pressure signals is expected or observed. Again, comparison of simulation and experiment indicates that the observed interior pressures are very well reproduced.

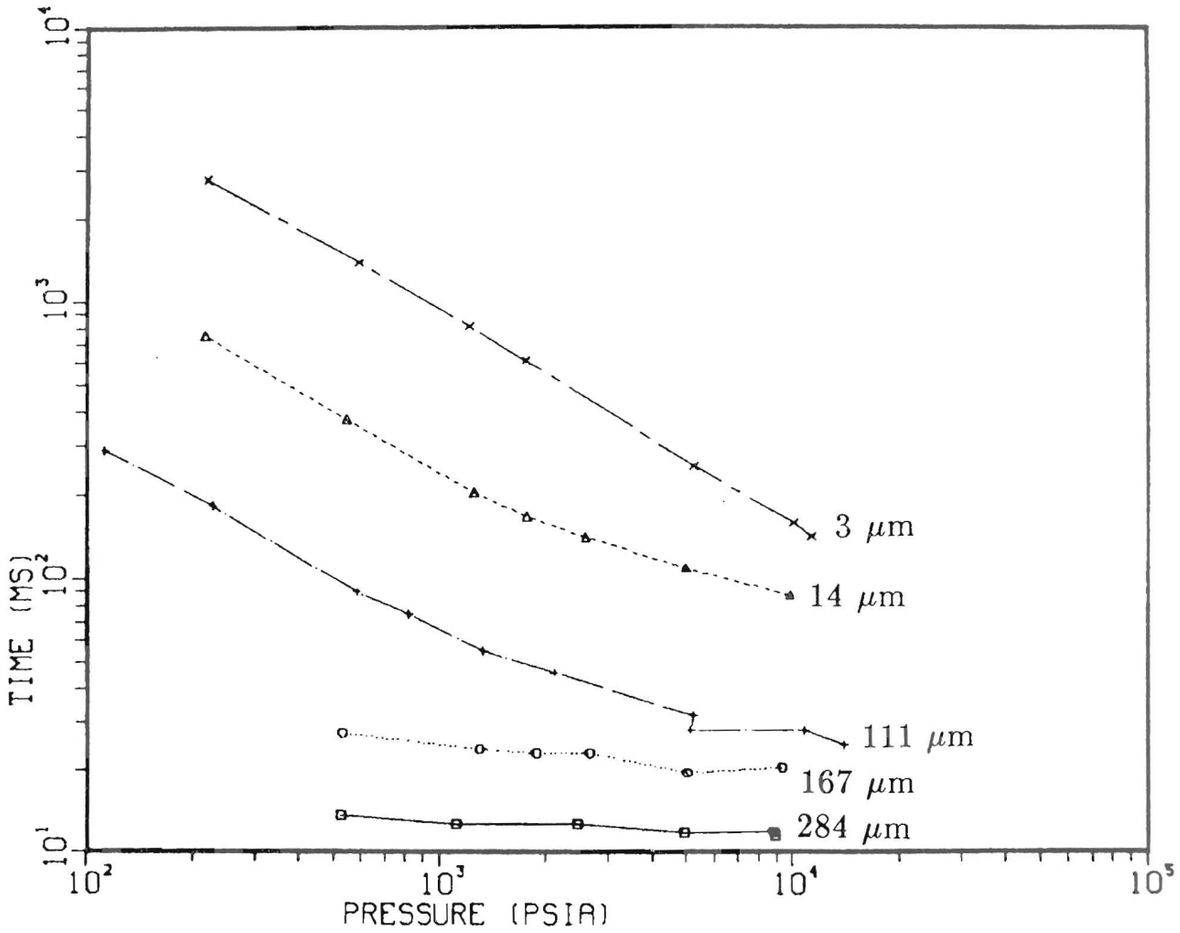

Figure 22: Experimental transit times t_d *vs* driving pressure ΔP. Data from glass bead packed beds.

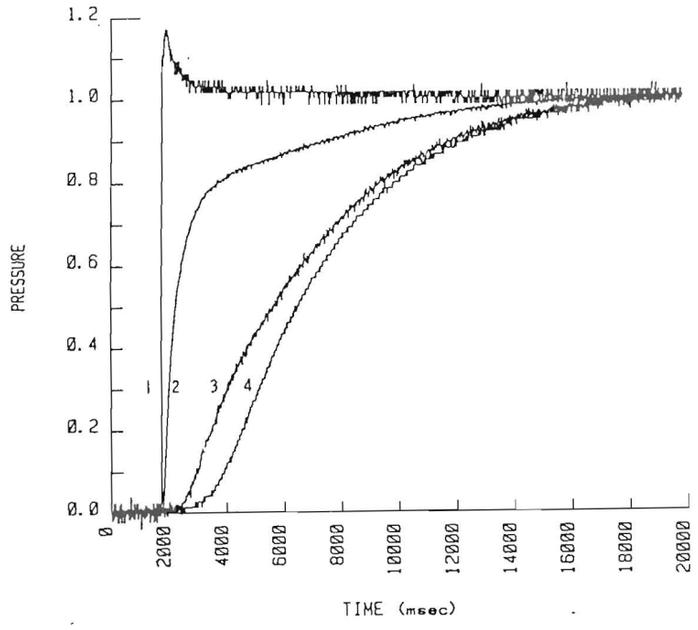

(a)

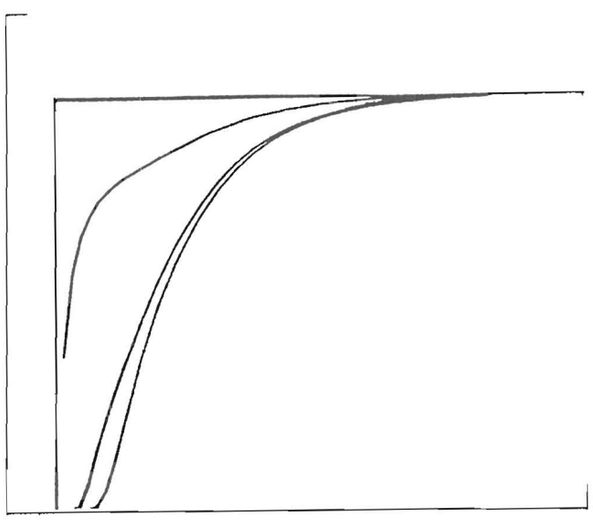

(b)

Figure 23: Experimental (a) and simulated (b) pressure waveforms at low Reynolds number in a packed bed of $CaCrO_4$. Effective particle size of 1.4 μm, $\mathcal{R} = 10^{-4}$, $\Delta P =$ 155 psia. Simulation results from the numerical (MOL) solution of the scaled equations.

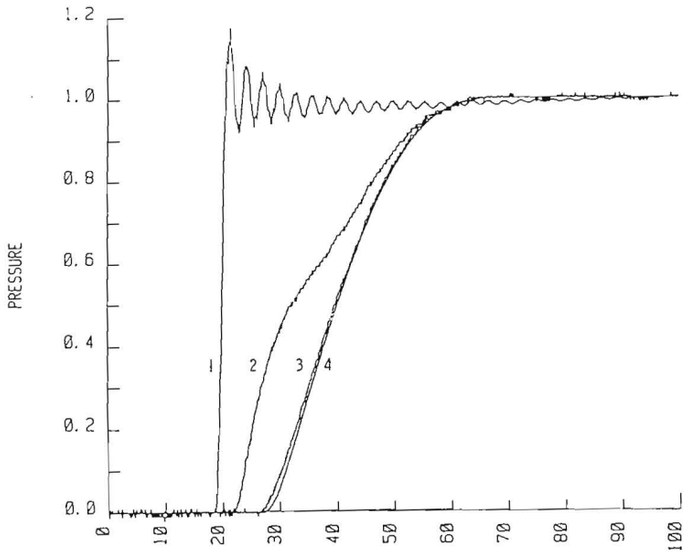

(a)

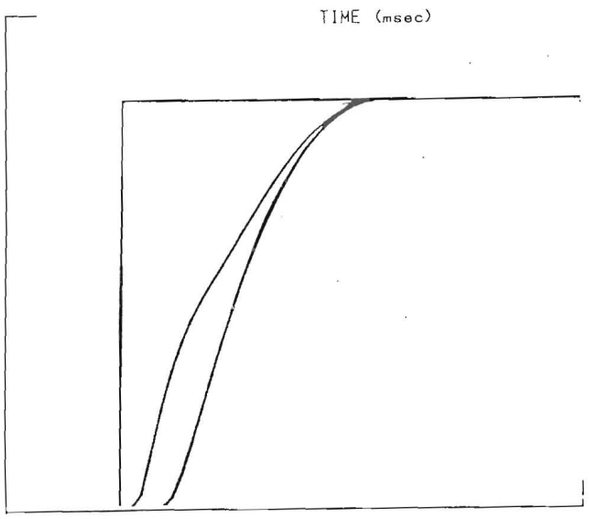

(b)

Figure 24: Experimental (a) and simulated (b) pressure waveforms at intermediate Reynolds number in a packed bed of glass beads. Mean bead diameter of 10 μm, $\mathcal{R} = 2$, $\Delta P = 4900$ psi. Simulation results from the numerical (MOL) solution of the scaled equations.

7 Summary

An experimental investigation of transient compressible flow in porous materials is reported. Two types of experiments have been carried out to verify the simplified models of compressible flow that have been developed by other investigators over the last decade and to extend the drag coefficient measurements to high Reynolds numbers. Results are reported for packed beds constructed from glass beads and three types of granular explosives: CP, HMX, and HNS.

In the first type of experiment, a reservoir of high-pressure nitrogen gas was discharged through packed beds of both inert and explosive materials. We show that after an initial transient, the gas flow becomes quasi-steady and the drag coefficient can be deduced from the pressure-time history of the reservoir gas. Using this technique, the drag coefficient can be determined over a large range of Reynolds numbers in a single test. Results are reported for Reynolds numbers from 10^{-4} to 10^{5} and compared with the conventional drag coefficients reported by previous investigators.

Previous correlations based on beds packed from spherical particles are compared with our results. The glass bead data agree well with either the classic Carman-Kozeny formula or Rumpf and Gupte's empirical correlation. Both correlations overpredict the permeabilities of CP by a factor of 5-50. The porosity dependence of the Rumpfe-Gupte correlations appears to fit the data better than the Carman-Kozeny expression.

In the second type of experiment, a miniature shock tube has been used to impulsively apply nitrogen gas at pressures from 100 to 20,000 psia to a bed of packed glass beads instrumented with pressure transducers. Glass beads with mean diameters ranging from 5 to 300 μm were used. The results of these experiments are compared to numerical solutions of the proposed model equations and simple analytic models that result at large and small Reynolds numbers. Both pulse shape and transit time show satisfactory agreement with the theory.

8 References

1. F. A. L. Dullien, 1979, **Porous Media**, Academic Press, NY, NY.

2. I. F. MacDonald, M. S. El-Sayed, K. Mow, and F. A. L. Dullien, 1979, "Flow through Porous Media – The Ergun Equation Revisited," *Ind. Eng. Chem. Fundam.* **18**, 199-208.

3. H. Rumpf and A. R. Gupte, 1971, "Einflüsse der Porosität und Korngroßenverteilung im Widerstandsgesetz der Porenströmung," *Chem. Ing. Tech.* **43**, 367-375.

4. P. L. Stanton, E. A. Igel, L. M. Lee, J. M. Mohler, and G. T. West, 1981, "Charcterization of the DDT Explosive CP," in *Proceedings of the 7th Symposium (In-*

ternational) on Detonation, Naval Surface Weapons Center Report NSWC MP 82-334.

5. M. R. Baer, E. A. Igel, J. W. Nunziato, and R. J. Gross, 1983, *A Study of Deflagration-to-Detonation Transition (DDT) in the Granular Explosive, CP* Sandia National Laboratories Report SAND83-1929.

6. B. N. Griffiths and J. M. Groocock, 1960, "The Burning to Detonation of Solid Explosives," *J. Chemical Society*, London, 4154.

7. Quantimet is an automatic particle sizing and counting apparatus. K. Varga performed this analysis.

8. F. A. Morrison, Jr., 1972, "Transient Gas Flow in a Porous Column," *Ind. Eng. Chem. Fundam.* **11**, 191-197.

9. F. A. Morrison, Jr., 1976, "Similarity in Transient High Speed Gas Flow Through Porous Media," *J. Fluids Eng.* **98**, 567–568.

10. F. A. Morrison, Jr., 1977, "Transient Non–Darcy Gas Flow in a Finite Porous Bed," *J. Fluids Eng.* **99**, 779–781.

11. R. H. Nilson, 1981, "Transient Flow in Porous Media: Inertia–Dominated to Vicous–Dominated Transition," *J. Fluids Eng.* **103**, 339–343.

12. J. M. Hyman, 1979, "MOL1D: A General Purpose Subroutine Package for Numerical Solution of Partial Differential Equations," Los Alamos Scientific Laboratory report LA-7595-M.

DISTRIBUTION:
UC-45 (31)

A. G. Butcher
Hercules, Inc.
Aerospace Division, MS.J12D
P.O. Box 98
Magna, UT 84044

P. Barry Butler
Department of Mechanical Engineering
The University of Iowa
Iowa City, IA 52242

M. Cowperthwaite
SRI International
Menlo Park, CA 94025

DOE Albuquerque Operations Office
N. S. Dienes, Productions Operations Div.
Acting Director, Weapons Program Div.
Albuquerque, NM 87185

W. Elban
Loyola College
Dept. of Eng. Science
4501 N. Charles St.
Baltimore, MD 21210

Explosive Technology
P. O. Box KK
Fairfield, CA 94533-0659
J. E. Kennedy

Douglas E. Kooker
U.S. Army Ballistic Research Laboratory
AMXBR-IBD
Aberdeen Proving Ground, MD 21005-5066

Kenneth K. Kuo
Dept. of Mechanical Engineering
The Pennsylvania State University
University Park, PA 16802

Lawrence Livermore National Laboratory (3)
P. O. Box 808
Livermore, CA 94550
M. Costantino, L-324
E. L. Lee, L-368
C. M. Tarver, L-368

Lockheed EMSCO
P. O. Drawer MM
Las Cruces, NM 88004
C. V. Bishop

Los Alamos National Laboratory (5)
Los Alamos, NM 87545
W. C. Davis, MS960
J. J. Dick, P952
J. McAfee, J960
R. Rabie, M-9
P. Sheffield, P952

McGill University (2)
Mechanical Engineering Department
817 Sherbrooke
Montreal, Quebec H3A-2K6
CANADA
J. H. Lee
R. Knystautas

Military Engineering Section
Defense Research Estab. Suffield
Ralston, Alberta T0J 2N0
CANADA
I. O. Moen

H. Moulard
Franco-German Research Inst.
P.O. Box 301 Saint Louis 68301
France (ISL)

Naval Weapons Center (3)
China Lake, CA 93555
C. F. Price, Code 389
T. L. Boggs, Code 389
A. Atwood, Code 389

R. H. Nilson
S-Cube
P.O. Box 1620
LoJolla, CA 92038

Elaine Oran
NRL
Code 4040
Naval Research Lab
Washington, D.C. 20375

Rensselaer Polytechnic Institute (10)
Dept. of Mechanical Engineering,
Aeronautical Engineering and Mechanics
Ricketts 104
Troy, NY 12180-3590
J. E. Shepherd

Dr. Roger Strehlow
505 South Pine Street
Champaign, IL 61820

University of Connecticut
Dept. of Mechanical Engineering
191 Auditorium Road
Storrs, CT 06268
Eli K. Dabora

University of Illinois
Dept. of Mechanical Engineering
Urbana, IL 61801
H. Krier

University of Illinois
Dept. of Theoretical and Applied Mechanics
Urbana, IL 61801
D. Scott Stewart

University of Michigan
Dept. of Aerospace Engineering
Ann Arbor, MI 47109
Martin Sichel

H. J. Verbeek
Prins Maurits Laboratorium TNO
Postbus 45, 2280 AA Rijswijk ZH
The Nederlands

Albert M. Weston
Brobeck Corporaton
1235 Tenth Street
Berkeley, CA 94710-1593

White Oak Laboratory (3)
Naval Surface Weapons Center
10901 New Hampshire Ave.
Silver Spring, MD 20903-5000
Richard R. Bernecker, R13
Kibong Kim, R13
Harold W. Sandusky, R13

Whiteshell Nuclear Research Establishment
Pinawa, Manitoba, ROE-1LO
CANADA
David J. Wren

Internal Distribution:

1510 J. W. Nunziato
1511 D. K. Gartling
1511 L. A. Mondy
1512 J. C. Cummings
1512 M. R. Baer
1512 D. A. Benson
1512 K. L. Erickson
1512 A. S. Geller
1512 R. D. Skocypec
1513 D. W. Larson
1520 C. W. Peterson
1530 L. W. Davison
1550 R. C. Maydew
2510 D. H. Anderson
2512 J. G. Harlan
2512 D. R. Begeal (10)
2513 D. E. Mitchell
2514 L. L. Bonzon
2514 P. L. Stanton
2515 P. D. Wilcox
2515 A. M. Renlund
3141 S. A. Landenberger (5)
3151 W. L. Garner (3)
6420 J. V. Walker
6425 R. W. Ostensen
6427 M. Berman (3)
6427 S. E. Slezack
6427 D. W. Stamps
6427 S. R. Tieszen
7556 D. A. Nissen
8244 C. M. Hartwig
8244 S. K. Griffiths
8244 B. A. Meyer
8245 W. Hermina
8245 R. J. Kee
8361 D. R. Hardesty
8363 B. R. Sanders
8524 P. W. Dean